Tilmann, F., Grevemeiyer, I., Flueh, E. R., Dahm, T., Gossler, J. (2008): Seismicity in the outer rise offshore southern Chile: Indication of fluid effects in crust and mantle. - Earth and Planetary Science Letters, 269, 1-2, 41-55.

https://doi.org/10.1016/j.epsl.2008.01.044

Earth Planetary Science Letters xx (2008) xxx xxx doi:10.1016/j.epsl.2008.01.04
Author-prepared layout

Seismicity in the outer rise offshore southern Chile: indication of fluid effects in crust and mantle

Frederik J. Tilmann, [a,*] Ingo Grevemeyer, [b] Ernst R. Flueh, [b] Torsten Dahm, [c] Jürgen Goßler [b]

[a] *Bullard Laboratories, University of Cambridge, Cambridge CB3 0EZ, UK*
[b] *IfM-GEOMAR, Kiel, Germany*
[c] *Institute for Geophysics, University of Hamburg, Hamburg, Germany*

Received 24 July 20 07; revised 17 January 2008; accepted 22 January 2008 Editor: R. D. van der Hilst

Abstract

We examine the micro-earthquake seismicity recorded by two temporary arrays of ocean bottom seismometers on the outer rise offshore southern Chile on young oceanic plate of ages 14 Ma and 6 Ma, respectively. The arrays were in operation from December 2004-January 2005 and consisted of 17 instruments and 12 instruments, respectively. Approximately 10 locatable events per day were recorded by each of the arrays. The catalogue, which is complete for magnitudes above 1.2-1.5, is characterized by a high b value, i.e., a high ratio of small to large events, and the data set is remarkable in that a large proportion of the events form clusters whose members show a high degree of waveform similarity. The largest cluster thus identified consisted of 27 similar events (average inter-event correlation coefficient>0.8 for a 9.5 s window), and waveform similarity persists far into the coda. Inter-event spacing is irregular, but very short waiting times of a few minutes are far more common than expected from a Poisson distribution. Seismicity with these features (high b value, large number of similar events with short waiting times) is typical of swarm activity, which, based on empirical evidence and theoretical considerations, is generally thought to be driven by fluid pressure variations. Because no pronounced outer rise bulge exists on the very young plate in the study region, it is unlikely that melt is accessible from decompression melting or opening of cracks. A fluid source related to processes at the nearby ridge is conceivable for the younger segment but less likely for the older one. We infer that the fluid source could be seawater, which enters through fractures in the crust. Most of the similar-earthquake clusters are within the crust, but some of them locate significantly below the Moho. If our interpretation is correct, this implies that water is present within the mantle. Hydration of the mantle is also indicated by a decrease of P_n velocities below the outer rise seen on a refraction profile through one of the arrays (Contreras-Reyes et al., 2007). The deepest events within the array on the 6 Ma old plate occur where the temperature reaches 500-600°C, consistent with the value observed for large intraplate earthquakes within the mantle (650°C), suggesting that the maximum temperature at which these fluid-mediated micro-earthquakes can occur is similar or identical to that of large earthquakes.

Key words: subduction, outer rise, seismicity, fluids and earthquakes, serpentinization
PACS: 91.30.Dk, 91.30.Ga, 91.30.Ye, 91.50.Wy, 91.55.Tt

1. Introduction

The outer rise forms an integral part of the subduction system with regard to both material fluxes and stress distribution. The oceanic lithosphere is stressed by bending and remote loading from the subduction zone or possibly other nearby plate boundaries, so that crustal and even mantle earthquakes occur. Faulting at the outer rise is thought to provide pathways for water into the lithosphere, both its crustal part (Kirby et al., 1996) and probably also into the mantle (Ranero et al., 2003; Ranero and Sallares, 2004; Grevemeyer et al., 2007); it therefore exerts a strong influence on melt generation and rheology further down the subduction system. Hydration of the mantle lithosphere at the outer rise can potentially more than double the amount of water carried by the downgoing slab (Rüpke et al., 2004). Dehydration of serpentinised mantle has also been proposed to account for the lower plane of double seismic zones (Peacock, 2001). The stress field at the outer rise is a superposition of bending stresses and regional horizontal stresses (Christensen and Ruff, 1988). Because the latter varies

* Corresponding author
Email address: tilmann@esc.cam.ac.uk (Frederik J. Tilmann,).

through the seismic cycle of the interplate megathrust (e.g. Taylor et al., 1996), with trench-perpendicular compression late in the cycle and tension early in the cycle, Christensen and Ruff (1988) proposed that an increased numbers of outer rise thrust events indicates an interplate-thrust close to the rupture limit, whereas many normal faulting events are expected to follow great interplate earthquakes. However, actual mechanisms also depend on the loading history (Mueller et al., 1996), such that the relationship is likely to be more complicated than suggested by this simple idea.

In addition to its significance to the subduction system, the outer rise region also plays host to most of the world's oceanic intraplate seismicity (excluding intermediate and deep-focus earthquakes which might be controlled by different frictional laws). Intra-plate earthquakes in oceanic mantle have been used to show that temperature is the dominant factor controlling the depth of brittle faulting (Wiens and Stein, 1983), with 650°C being the maximum temperature at which earthquakes are observed (McKenzie et al., 2005). However, all previous studies of outer rise seismicity and oceanic intraplate seismicity in general exclusively utilised teleseismic and regional data (e.g. Wiens and Stein, 1983; Christensen and Ruff, 1988). This approach allows global coverage but limits the analysis to strong earthquakes ($m_b >\sim 5.5$). This limitation poses particular problems for very young oceanic plates where few events of sufficient magnitude occur. Moreover, the finite source properties of the larger of these events make it hard to ascertain the maximum depth of faulting (as opposed to the hypocentre, see Tichelaar et al. (1992)). Here, we take the complementary approach and use dense arrays of ocean bottom stations to characterize micro-earthquake activity in the outer rise of the Chilean subduction zone.

A number of fracture zones north of the Chile triple junction segment the Nazca plate which subducts at the Chilean margin (Figure 1). No significant variation has been resolved in the convergence rate between the Nazca and South American plates (7.9 - 8.0 cm/yr, near trench-perpendicular convergence of N79E) (DeMets et al., 1994). However, the square root of time dependence of plate cooling is expected to cause large variations of thermal structure. During cruise SO181 of R/V Sonne (December 2004-February 2005) we have placed seismic arrays on the second and third youngest subducting segments (with ages at the trench of 6 and 14 Ma at the centre of the segment, respectively), which are bounded, from south to north by the Guamblin, Guafo and Chiloe fracture zones. This experiment forms part of the TIPTEQ project (Scherwath et al., 2006), so that the passive seismic data are complemented by refraction and heat flow profiles as well as swath bathymetry mapping and magnetic profiling.

2. Data and processing

The northern array consisted of 7 ocean bottom hydrophones (OBH) and 10 four-component stations (ocean bottom seismometers - OBS). The southern array consisted of 2 OBH and 10 OBS. All stations were sampling continuously at 100 Hz, except obh28 within the southern array which sampled at 50 Hz. Most stations were operational for 5–6 weeks, but two stations, one in each array, did not return any useful data (see Table S1 in the supplementary material for station locations and instrument types). The hydrophone records generally showed clear P onsets and, for most stations, could easily be picked on the unfiltered traces (Figure 2). Strong S arrivals were visible on all seismometer components (including the vertical) but were characterized by ringing, nearly monochromatic waveforms, presumably due to resonances within the shallow sediment. The P arrivals on the hydrophone channels were usually succeeded by a strong arrival on the seismometer channels 0.5–1 s later, with the time delay varying from station to station but being similar between events. Similarly, S arrivals were preceded by precursory arrivals, which were particularly clear on the hydrophone channels, but sometimes also appeared weakly on the horizontal components, again separated by approximately 0.5–1 s from the main arrival. The delayed and precursory phases are presumably related to mode-conversions at the basement. Active source data show that sediment thickness does not exceed 500 m in the area of the array (Flueh and Grevemeyer, 2005; Contreras-Reyes et al., 2007) but the observed large delays are easily explained by extremely low S velocities (<100 m/s) in the uppermost layers of unconsolidated marine sediment (Hamilton, 1980).

2.1. *Location and magnitude determination*

Before any further analysis, timing and location of the ocean bottom stations were corrected as described in the supplementary material. We then carried out the following procedure.

(i) Generation of a preliminary list of events with a STA/LTA trigger algorithm that detects nearly coincident changes in the amplitude at several stations.

(ii) Manually inspect all trigger events and pick arrivals, assigning a subjective weight to each pick. Remove events, which are unclear, presumably not earthquakes, or cannot be picked on at least three stations.

(iii) Obtain a preliminary location for each event by linearised inversion and using a 1-D velocity model derived from the refraction data (Scherwath et al., 2006). A total of 656 events were located by the northern array, and 1114 events by the southern array.

(iv) Based on preliminary locations, temporarily remove events which were recorded by less than 5 stations, have only picks for one phase type (P or S), or are far from the array (azimuthal gap > 300°). This procedure leaves 240 events for the northern array, and 484 events for the southern array. In the following we will refer to these events as the restricted set or restricted

events.

(v) Apply the joint hypocentre determination (JHD) method to the restricted event sets (using VELEST (Kissling et al., 1994)). Station delays for S were large ($\sim$ 1s) and did not correlate well with P delays but instead correlated with the observed delays between the P arrival and the delayed phase, and between the S-precursor and main S arrival. This observation is consistent with our interpretation of a zone of extremely low S velocities causing much of the delay between direct and mode-converted phases.

(vi) For the southern array only, we further restrict the data set to those events with a gap of less than 200° and eliminating outlier picks with residuals larger than 0.75 s (after JHD). This procedure leaves 287 events. A minimum 1D-model is determined for this event set (Kissling et al., 1994) (see Figure S2 in the supplementary material for velocity model). We tested the robustness of the minimum-1D model by randomly perturbing the starting model and comparing the resulting models and depth distributions. Only slight differences in average event depths are found (<1 km). Similarly, even with extreme variations in starting event depths, the resulting final depth distributions and models are similar.
Most of the events were located at the margin or outside the northern array, so that a minimum-1D model could not be determined. However, the velocity structure of the northern array is constrained by both trench-parallel and -perpendicular refraction lines (Contreras-Reyes et al., 2007, 2008) such that the lack of a minimum-1D model in the north should not compromise our ability to determine accurate locations.

(vii) Using the station terms and, in the south, minimum 1D-model (Table S1, Figure S2 in supplementary material) derived in the previous two steps we relocate all earthquakes using the non-linear oct-tree search algorithm (Lomax et al., 2000). This method efficiently explores the probability density function for the location associated with a particular earthquake, and as such provides much better information on location errors than linearised inversions. The maximum-likelihood location is retained as the catalogue location.

(viii) Finally, moment magnitudes are estimated using the automated procedure of Ottemöller and Havskov (2003), which was modified to account for the requirements of the ocean bottom data (see supplementary material for further information).

2.2. *Correlation and cluster identification*

We cross-correlate the waveforms from all events. In many cases, an extremely high degree of waveform similarity is observed between the traces of different events, with correlation coefficients as high as 0.95 for a correlation window of 9.5 s, equivalent to more than 60 oscillations at the dominant period of the data (Figure 3a). We identify all events with similar waveforms and group them into clusters using hierarchical average-linkage clustering with the dendrogram method (Hartigan, 1975). During the deployment period, 41% of events within the southern array exhibited a high degree of waveform similarity (average correlation coefficient larger than 0.8) with at least one other event, with the largest cluster encompassing 27 events (Figure 3c). For the northern array, 32% of events are members of a cluster, and the largest cluster consisted of 11 events (Figure 3b). Within both arrays, doublets were the most common type of cluster.

For all identified clusters, cross-correlation time differences are evaluated using a short window of 0.4 s for the P arrival and 0.6 s for the S wave (with lead-in times before the P or S pick of 0.1 and 0.2 s, respectively). The short time window minimises the impact of scattered arrivals, while the restriction of correlation time measurements to known clusters eliminates the possibility of obtaining spurious measurements with high correlation coefficients which otherwise are expected to occur by chance for short time windows. All events are relocated using the double-difference procedure (Waldhauser and Ellsworth, 2000) with both catalogue and correlation times but only approximately half the events are sufficiently linked to neighbouring events to be included in the double-difference inversion (see Figure 4).

A cluster location for all clusters of three or more events is derived by first aligning the waveforms, and then using the median of the manual picks of individual events as the cluster arrival time. This procedure also allows an independent verification of the manual picking errors. If we define the picking error as the difference between the earliest and latest pick within a nearly identical waveform, the average picking error for P is 0.06-0.10 s (maximum: 0.58-0.77 s) and the average error for S is 0.09-0.10 s (maximum 0.38-0.88 s); the lower bounds pertain to the southern array and the upper bounds to the northern array. It has to be remembered that these picking errors are only valid for identified clustered events and might not be representative of the overall dataset.

Lastly, for all those cluster locations with small azimuthal gaps and good depth constraints we pick the polarity of arrivals on the hydrophone component. The ability to view nearly-identical signals on several traces strongly reduces the likelihood of misidentifications of polarities due to the presence of noise. The station density is not high enough to determine reliable focal mechanism solutions for individual clusters but an estimate of the regional stress field was made using the method of Robinson and McGinty (2000), which attempts to fit the first motions of all earthquakes simulataneously by varying the direction of the regional P and T axes and using the assumptions that earthquakes occur on optimally oriented fault planes. Because bending might cause a variation of the 'regional' stress with depth,

we separate the event set into shallow crustal (<4 km below the seafloor) and deep crustal/mantle earthquakes (>4 km below the seafloor).

Because most of the activity in the north is just outside the array, the first motions do not provide a meaningful constraint on the stress field there and were not picked.

3. Results

3.1. *Epicentres and magnitude distribution*

The seismic activity recorded by the northern array is strongly concentrated in a small area of about 10×20 km^2 (Figure 4a). Mean event rates within this sub-area dropped sharply from 10 events per day to 1.7 per day on December 23 (event rates only take into account events that are in the restricted set and have magnitude determinations). As outside this region events occurred at a nearly constant rate of 2.3 events per day throughout the experiment, and no changes to the network configuration took place near December 23 we probably witnessed the tail end of an earthquake swarm with event magnitudes up to M_W=2.7, but no clear mainshock-aftershock sequences. Even after December 23, the swarm region remained the most active region in terms of number of events per area.

In contrast, no single region dominates in the southern array, and the event rate is ∼10 events/day throughout. Some events form elongated groups that are aligned subparallel to the pre-existing fabric; however, the clearest of these groups, between obh19 and obs24 (Figure 4b), actually subtends an angle of nearly 20° with pre-existing seafloor fabric.

The frequency-magnitude distribution (Figure 5) of events in both sub-arrays is characterized by β values (slope of frequency-log(M_0) plot) between 1.0 and 1.1 for the northern and southern array, respectively, equivalent to b values (for M_W) of 1.5 and 1.7. There is some suggestion in Figure 5 that the b value of the northern array is biased upwards by the swarm activity, but the number of earthquakes outside the swarm region is too small for a reliable estimate. The magnitude of completeness M_c differs by 0.4 magnitude units between the southern and northern arrays. The greater sensitivity of the southern array is a sufficient explanation for the larger total number of events recorded by it. In fact, event rates for events with $1.5 < M_W < 2.5$ are very similar for both arrays if the swarm region in the northern area is excluded. Given comparable station densitities within both arrays, the cause of the different sensitivities is not clear; possibly, it is related to the spatial distribution of seismicity: for the southern array, most earthquakes are shallow and within the array; for the northern array, the average earthquake depth is larger, and most earthquakes occur outside the array. In the southern array, small earthquakes are thus more likely to be recorded by a sufficient number of stations to be included in the restricted set. An alternative explanation for the apparent different M_c values could be a systematic difference in the average station amplification factors (see supplementary material) of both arrays. This explanation would imply that seismicity rates are indeed larger for the southern array. A direct comparison of the magnitude estimates for the only two events recorded by both arrays does indeed show a systematic shift consistent with the latter explanation but uncertainties are too large to be conclusive.

3.2. *Event depths*

Within both arrays, most earthquakes occur within the crust but both also show significant activity in the mantle (Figures 6 and 7). Within the southern array, the deepest well-located events occur at a depth of ∼10 km (Figure 6) below the seafloor, only slightly deeper than the maximum depth of faulting at slow-spreading ridges (e.g. Toomey et al., 1988; Tilmann et al., 2004). Asssuming purely conductive cooling, this depth corresponds to temperatures of 500-600°C, although hydrothermal activity near the ridge or at the outer rise could result in somewhat lower temperatures. We find a larger fraction of deep events in the region of the northern array (Figure 7) but a more quantitative comparison is precluded by the small number of events with well-constrained depths in the north. A later array deployment landward of the trench located intra-oceanic-plate earthquakes in the trench region of this segment (75.5°W) with a maximum depth of ∼30 km (Lange et al., 2007).

3.2.1. *Uncertainties of hypocentral determinations*

In order to evaluate the significance of the earthquake depth distribution and possible alignment of epicentres, we need to be sure what the uncertainties are. We consider particularly the uncertainties of the events with robust depth determinations, which are plotted in Figure 6a and are represented by coloured circles in Figure 4. Events within this set have at least 5 readings, an azimuthal gap of less than 200°, a minimum probability at the maximum likelihood location of 0.05, a traveltime rms of less than 0.4 s, and a maximum length of 2.5 km for the longest semi-axis of the 68% confidence ellipsoid. Formal error estimates are derived from the probability density functions. The median and maximum horizontal standard deviations are 0.7 km and 2.1 km, respectively, with little difference in the NS and EW directions. The median and maximum vertical standard deviations are 1.8 km and 2.5 km, respectively, where the maximum bound is imposed by the selection criteria just described. The probability density functions for one shallow and two deep events are shown in Figure 6b. Most other events in the set have comparable location uncertainties. As expected, events within the array have a nearly circular confidence region for the epicentre, making it highly unlikely that the alignment of epicentres which is visible for some groups of events in Figure 4 is an artifact of location uncertainties. The confidence ellipsoids are generally

elongated in the vertical direction, with the 95% confidence shallow limit for the deeper events falling near the Moho. In spite of this, we believe the occurrence of events in the mantle to be a robust feature. The deep groups are well separated from groups of shallower events, and therefore for these events to be above Moho, the true location for *all* these events would have to be at the upper limit of the 95% confidence region, a very unlikely proposition. However, the apparent near-vertical alignment of some groups visible at profile distances of 70-65 km in Figure 6 could feasibly have resulted from smearing due to mislocations of events within much tighter clusters.

3.3. *Cluster analysis*

The location of cluster events appears to reflect the overall distribution of seismicity. They are distributed through the experimental region in the south, and are strongly concentrated within the swarm region in the north (Figure 8). In particular, cluster type events occur both within the crust and mantle in the southern area. Within the northern area, the fact that most clusters locate outside or at the limit of the array and therefore have poor depth determination precludes us from making a similar assertion about the northern area. Short intervals between events belonging to the same cluster are common, with occasional reactivation after a longer waiting time. In fact, the recurrence interval distribution follows a power-law (Figure 9a), which indicates that the individual events of a cluster do neither occur independently of each other, nor do they seem to recur at quasi-periodic intervals. The deficit of events at very short recurrence intervals (below $\sim$100s) could possibly have arisen from our processing method which would miss events occurring in the coda of a previous event.

The events within a cluster can differ in magnitude by up to one magnitude unit, but inspection shows that the largest events of any cluster do not occur preferentially at or near the beginning of the sequence, i.e. they cannot be understood in terms of a mainshock with its aftershocks. This is also likely to be true when considering the swarm in the northern array where the largest event occurs close to the end of the sequence (Figure 9b). We cannot categorically exclude a large earthquake before the beginning of our survey (but small enough not to be registered teleseismically), but the abrupt end of the swarm argues against its interpretation as an aftershock sequence.

3.4. *Stress directions*

The stress fields estimated from the shallow and deep event set within the southern array are both characterized by a sub-horizontal EW to ENE-WSW oriented pressure axis but differ in the orientation of the tension axis (Figure 10). However, the uncertainty regions of both sets overlap, and fitting the whole dataset results in stress direction estimates very similar to those of the shallow set (σ_1 az=260°, dip=10°; σ_3 azimuth=350°, dip=0°;) with only marginally reduced fit (%ok[polarities fit]=92.9). Although mechanism types for individual clusters could not be determined with any confidence the results were also generally compatible with EW compressional stresses, and were generally *not* compatible with EW tensional stresses.

4. Discussion

Large b values are typically found in volcanic or geothermal areas, or in the creeping sections of faults (Wiemer and Wyss, 2002). Similarly, the presence of a large number of earthquakes with strong waveform similarity over a short time span is typical of swarm-like activity. Repeating earthquakes are also found in or near creeping sections of major faults (e.g., Nadeau and Johnson, 1998) but are then generally characterised by more regular, and larger, inter-event times, and smaller variation in event magnitudes within a cluster. Power law distributions of waiting times can also arise in settings where elastic stress transfer dominates, but in this case mainshock-aftershock sequences result in the largest earthquakes preferentially occuring near the beginning of a sequence, contrary to our observations (e.g., Figure 9b).

Swarm-type seismicity has been previously observed in the shallow crust following rainfall (Kraft et al., 2006), in the mid-crust in central Europe (Spičák and Horálek, 2001), in the mid- and upper-crust in California and Japan (Vidale et al., 2006), and in the crust of the overriding plate of the Aegean subduction zone (Becker et al., 2006) and other settings (e.g Chiaraluce et al., 2007). In all those examples, fluids have been implicated in causing the swarm seismicity, with Kraft et al. (2006) and Becker et al. (2006) reporting a similar distribution of multiplet sizes to the one observed here, i.e., a dominance of doublets, with a few multiplets with many events. Yamashita (1999) has developed a model which explains how the presence of fluids can lead to swarm type activity if the rate of pore creation is large. In his model, overpressures within a fault allow earthquakes to occur. As the earthquake progresses, permeability is created within the fault zone, which allows the overpressures to diffuse away, thereby arresting the earthquake before it becomes too large. In this way mainshock-aftershock sequences are suppressed, and smaller events are more common.

The dramatic rate change within the northern array hints that swarm activity does indeed occur within our study region. However, the presence of earthquakes with similar waveforms outside the area of this particular swarm as well as the fact that a high rate of similar earthquakes is observed in both arrays within two different segments of the incoming plate strongly suggests that this type of seismic activity is typical for the outer rise region in Southern Chile, rather than just a fortuitous recording of a rare swarm event.

Based on the occurence of cluster events up to 8-9 km

below the seafloor (for a ∼5 km crust), we thus infer the presence of fluids within both the crust and the mantle below our southern array on the 6 Ma old plate. Although the database in the northern array is weaker with regard to hypocentral depth, it seems reasonable to assume that cluster events occur at least as deep as below the southern array. We will now consider potential fluid sources.

(i) Melts. Minor magmatism has been observed on the outer rise of old plates (Hirano et al., 2004), and has been attributed to melts prevalent in the asthenosphere, which can migrate to the surface following flexure-induced fracturing (Hirano et al., 2006). However, observations of velocities in the low velocity zone below the oceans in conjunction with measurements of the temperature dependence of seismic velocities at seismic frequencies indicate temperatures below the solidus, and in particular do not indicate the presence of melt (Faul and Jackson, 2005; Priestley and McKenzie, 2006). Furthermore, the elastic thickness of very young plates is expected to be small, particularly at 6 Ma, and thus little flexure should occur. This is borne out by the absence of an identifiable flexural bulge in either topography or gravity (e.g. Bry and White, 2007). We thus do not consider it likely that the fluids implied by the seismicity are pervasive asthenospheric melts. The fluids are also unlikely to be remnant melt advected with the plate from the ridge axis because even at 6 Ma, a magma-filled sill or dike formed at the ridge would need to be several kilometres thick in order to escape solidification (Turcotte and Schubert, 2002). Volatiles related to processes at the ridge might feasibly remain in the crust, and maybe even the mantle, and could influence the seismic activity at the outer rise. However, the apparent similarity of clustering behaviour in the 14 Ma and 6 Ma old plates argues against a strong influence of the ridge on our observations.

(ii) Water. As the minerals within the oceanic lithosphere experience no significant pressure change on approach to the outer rise area, it is not clear how water could be sourced from dehydration reactions. It is thus necessary to transport water into the seismically active region. One possibility is that seawater is penetrating along major faults as proposed by Peacock (2001) and Ranero et al. (2003). In order for this mechanism to be feasible, some basement outcrops are required to serve as inflow sites, as the sedimentary blanket tends to be relatively impermeable. Basement is exposed widely in the southern area (Figure 4b), but only isolated outcrops can be seen in the northern area (Figure 4a). However, Fisher et al. (2003) demonstrated that circulation cells can span surprisingly large lateral distances with up to 50 km between in- and outflow sites. Heat flow measurements have been collected in the northern area along a ∼10 km long trench-perpendicular profile (Contreras-Reyes et al., 2007, see Figure 4a for approximate location). The heat flow matches the expectation from a purely conductive model at the westernmost measuring point but is much lower than expected (by ∼60 mW/m^2) at the easternmost point; the heat flow measurements are well explained if the basement is cooled to near seabottom temperatures, proving that water enters the crust, similarly to what is observed in other outer rise areas with exposed basement in Nicaragua and Central Chile (Grevemeyer et al., 2005).

However, the heat flow measurement points are located ∼25 km seaward of the seismically active area and they cannot tell us how deep the water penetrates. A 250 km long trench-perpendicular refraction profile, approximately passing through obs03, obh06 and obh11, has been shot through the array (Contreras-Reyes et al., 2007). P_n velocities in the western part of this profile are 8.1 km/s and above as expected for oceanic upper mantle, but decrease to 7.8 km/s below the outer rise region, at a broadly similar distance to the trench where we observed the swarm activity (Figure 4a). A nearby trench-parallel profile recorded clear S waves, which indicated a large mantle Poisson ratio of 0.29 (Contreras-Reyes et al., 2008). The decrease of mantle seismic velocities below the outer rise can be explained by partial hydration of the mantle by serpentinisation (Carlson and Miller, 2003), and thus serves as an independent indicator that fluids can circulate down to mantle depths. Similar reductions of P_n velocities in the outer rise region have been observed in Northern Chile (Ranero and Sallares, 2004) and in Middle America (Grevemeyer et al., 2007). In the latter example, a small outer rise passive network (4 hydrophones) recorded a number of earthquakes, whose best fit solution was in the mantle but because of the small number of stations and the lack of S wave observations, depth error bars were generally too large to be certain, and it is not known whether those earthquakes showed similar clustering behaviour and a similarly large b value. Whereas we—in accordance with most of these papers—prefer an interpretation where seawater percolates from the seafloor, an alternative scenario envisages a deep source of water. The water released from the downgoing slab by dehydration reactions could partly remain in the slab and hydrate it (Abers et al., 2003; Robin and Robin, 2007), rather than percolating into the overriding plate, as is usually assumed. However, for this mechanism to serve as an effective source of mantle hydration the deep hydration front must move all the up to the surface, which would require the subduction zone to have been active for a very long time. It can also not explain the apparent coincidence of outer rise faulting and the onset of reduced Pn velocities. A trench-perpendicular refraction profile has also been collected within our southern array (Scherwath et al., 2006) but the interpretation of P_n velocities there is not straightforward

because a potential reduction of velocities due to serpentinisation is superimposed on a gradual velocity increase due to plate cooling.

The EW compressive stress direction inferred from the P wave first motions of some cluster events is opposite to the stress field expected for shallow events from bending. As the methodology (Robinson and McGinty, 2000) assumes a uniform stress field and imposes a constant value for the coefficient of friction, which are both essentially untestable assumptions, the reliability of the stress field inversion is uncertain but in any case the observed first motions cannot easily be reconciled with classic bending-related trench-perpendicular normal faulting. Given the small elastic thickness of the only 6 My old plate and the absence of a noticable outer rise bulge, we should probably not be surprised that the stress field is not primarily controlled by bending, as expected bending stresses would be small. Instead, we can expect regional tectonic stresses to be dominant, for example due to ridge push, or the progression of the seismic cycle on the megathrust (Christensen and Ruff, 1988). In particular, outer rise thrust events are thought to occur late in the seismic cycle. Although the megathrust landward of our southern array participated in the 1960 earthquake rupture, the inferred slip was less than half that of the slip maxima near the northern end of the rupture (Barrientos and Ward, 1990, also see Figure 1). It is thus entirely plausible that the southernmost part of the megathrust could have a slip deficit, which would put the adjacent oceanic plate into compression. However, the only three available Global CMT (centroid moment tensor) solutions (Dziewonski et al., 1981) in the southern area whose EHB location (Engdahl et al., 1998) puts them unambiguously on the outer rise all show normal faulting with an approximately trench-normal tension axis (Figure 1). These events are located landward of the micro-earthquakes examined by us, so it is possible that there is a change in stress regime as the plate approaches the trench and descends but without a more detailed study, beyond the scope of this work, we cannot exclude the possibility that the micro-earthquakes are simply not representative of the long-term, large scale stress field.

If our interpretation of the source of fluids is correct, it implies that hydration of slab mantle lithosphere can occur at the outer rise of even very young plates. Bending per se does not seem to be required, but the crust needs to be pervasively faulted to be able to act as a pathway for the water. The temperature at the hypocentre of the deepest earthquakes (500-600°C) is entirely consistent with McKenzie et al.'s (2005) recent estimates of the maximum temperature for brittle faulting in oceanic mantle (~ 650°C), which was inferred from the global dataset of intra-plate and outer rise events (Wiens and Stein, 1983), particularly given the small number of deep events in our dataset. It would thus appear that microearthquakes, even those triggered by fluids, cannot occur at temperatures substantially higher than those at which large earthquakes occur. This finding implies that the maximum depth of micro-earthquakes can be used to infer temperature structure; conversely, the presence of fluids (as invoked by, for example, Reyners et al., 2007) might not be sufficient to explain seismicity at locations thought to be too hot. This result is also consistent with the observation that the temperature limit of intermediate depth seismicity within subducting slabs, which is probably also related to fluid-effects (e.g., Peacock, 2001), is essentially identical to the limiting temperature for oceanic intraplate events (Emmerson and McKenzie, 2007).

5. Conclusion

Based on a temporary deployment of ocean bottom seismometers and hydrophones on the outer rise of two segments of the Nazca plate (14 Ma and 6 Ma old plate at the trench) as it is subducting at the Southern Chilean margin, we observe that micro-earthquakes occur throughout the crust and in the uppermost mantle. A significant part of the seismicity has the hallmarks of fluid-triggered seismicity, i.e., a large β value (>1) and a high degree of clustering with a large number of earthquakes with similar waveforms but irregular recurrence intervals and the absence of mainshock-aftershock patterns. The deepest earthquakes appear to occur at a temperature of 500-600°C, which, given the sampling, is consistent with the temperature limit of 650°C for large intra-plate earthquakes below the oceans. The triggering fluids could be derived from seawater, which enters the crust and mantle through pervasive faults, not necessarily bending-related. Corroborating evidence for the hydration of mantle lithosphere comes from a coincident refraction line through the array on the 14 Ma old plate (Contreras-Reyes et al., 2007), which shows a reduction of P_n velocity from more than 8.1 km/s to 7.8 km/s near the seaward limit of seismicity, projected along strike.

Acknowledgements

We thank Capts. Kull and Mallon and their crews for excellent suppport of the deployment. The SO181 shipboard scientific crew carried out initial processing of the data. We thank Martin Scherwath for providing detailed information on the data and for reading a draft of the manuscript. This is publication GEOTECH-284 of the R&D programme GEOTECHNOLOGIEN program funded by the German Ministry of Education&Research (BMBF) and German Research Foundation (DFG), grants 03G0181A and 03G0594E, and Cambridge Department of Earth Sciences Publication ES.9071. Comments by an anonymous reviewer helped to clarify the manuscript.

References

Abers, G., Plank, T., Hacker, B. R., 2003. The wet Nicaraguan slab. Geophys. Res. Let. 30 (2), 1098.

Aki, K., 1965. Maximum likelihood estimate of b in the formula log n = a-bm and its confidence limits. Bull. Earthq. Res. Inst. 43, 237–239.

Barrientos, S., Ward, S., 1990. The 1960 Chile earthquake: inversion for slip distribution from surface deformation. Geophys. J. Int. 103, 589–598.

Becker, D., Meier, T., Rische, M., Bohnhoff, M., Harjes, H.-P., 2006. Spatio-temporal microseismicity in the Cretan region. Tectonophys. 423, 3–16.

Brune, J., 1970. Tectonic stress and the spectra of seismic shear waves from earthquakes. J. Geophys. Res. 75, 4997–5009.

Bry, M., White, N., 2007. Reappraising elastic thickness variation at oceanic trenches. J. Geophys. Res. 112, B08414.

Carlson, R. L., Miller, D. J., 2003. Mantle wedge water contents estimated from seismic velocities in partially serpentinized periodotites. Geophys. Res. Let. 30 (5), 1250.

Chiaraluce, L., Chiarabba, C., Collettini, C., Piccinini, D., Cocco, M., 2007. Architecture and mechanics of an active low-angle normal fault:Alto Tiberina Fault, northern Apennines, Italy. J. Geophys. Res. 112, B10310.

Christensen, D. H., Ruff, L. J., 1988. Seismic coupling and outer rise earthquakes. J. Geophys. Res. 93 (B11), 13,421–13,444.

Contreras-Reyes, E., Grevemeyer, I., Flueh, E. R., Scherwath, M., Bialas, J., 2008. Effect of trench-outer rise bending-related faulting on seismic Poisson's ratio and mantle anisotropy: a case study offshore of Southern Central Chile. Geophys. J. Int.

Contreras-Reyes, E., Grevemeyer, I., Flueh, E. R., Scherwath, M., Heesemann, M., 2007. Alteration of the subducting oceanic lithosphere at the southern central Chile trench-outer rise. Geochem., Geophys. Geosyst. 8, Q07003.

DeMets, C., Gordon, R., Argus, D. F., Stein, S., 1994. Effect of recent revisions to the geomagnetic reversal time scale on estimates of current plate motions. Geophys. Res. Let. 21, 2191–2194.

Dziewonski, A. M., Chou, T.-A., Woodhouse, J. H., 1981. Determination of earthquake source parameters from wavefrom data for studies of global and regional seismicity. J. Geophys. Res. 86, 2825–2852.

Emmerson, B., McKenzie, D., 2007. Thermal structure and seismicity of subducting lithosphere. Phys. Earth Planet. Int. 163, 191–208.

Engdahl, E., van der Hilst, R. D., Buland, R. P., 1998. Global teleseismic earthquake relocation with improved travel times and procedures for depth determination. Bul. Seism. Soc. Am. 88, 722–743.

Faul, U. H., Jackson, I., 2005. The seismological signature of temperature and grain size variations in the upper mantle. Earth Planet. Sci. Let. 234 (1-2), 119–134.

Fisher, A. T., Davis, E. E., Hutnak, M., Spiess, V., Zühlsdorff, L., Cherkaoui, A., Christiansen, L., Edwards, K., Macdonald, R., Villinger, H., Mottl, M. J., Wheat, C. G., Becker, K., 2003. Hydrothermal recharge and discharge across 50 km guided by seamounts on a young ridge flank. Nature 421, 618–621.

Flueh, E. R., Grevemeyer, I. (Eds.), 2005. FS Sonne Cruise Report SO181 TIPTEQ. Vol. 2 of IFM-GEOMAR Report. Leibniz-Institut f. Meereswissenschaften an d. Christian-Albrechts-Universität Kiel.

Grevemeyer, I., Kaul, N., Diaz-Naveas, J. L., Villinger, H. W., Ranero, C. R., Reichert, C., 2005. Heat flow and bending-related faulting at subduction trenches: Case studies offshore of Nicaragua and Central Chile. Earth Planet. Sci. Let. 236, 238–248.

Grevemeyer, I., Ranero, C. R., Flueh, E. R., Kläschen, D., Bialas, J., 2007. Passive and active seismological study of bending-related faulting and mantle serpentinization at the Middle America trench. Earth Planet. Sci. Let. 258, 529–542.

Hamilton, E. L., 1980. Geoacoustic modelling of the sea floor. J. Acoust.. Soc. Am. 68, 1313–1340.

Hartigan, J. A., 1975. Clustering algorithms. Wiley, New York.

Hirano, N., Takahashi, E., Yamamoto, J., Abe, N., Ingle, S. P., Kaneoka, I., Hirata, T., Kimura, J.-I., Ishii, T., Ogawa, Y., Machida, S., Suyehiro, K., 2006. Volcanism in response to plate flexure. Science 313, 1426–1428.

Hirano, N., Yamamoto, J., Kagi, H., 2004. Young, olivine phenocryst-bearing alkali-basalt from the oceanward slope of the Japan trench. Contrib. Mineral. Petrol. 148, 47–54.

Kanamori, H., 1977. The energy release in great earthquakes. J. Geophys. Res. 82, 1981–1987.

Kirby, S., Engdahl, E. R., Denlinger, R., 1996. Intermediate-depth intraslab earthquakes and arc volcanism as physical expressions of crustal and uppermost mantle metamorphism in subducting slabs. In: et al., G. E. B. (Ed.), Subduction Top to Bottom. Vol. 96 of Geophys. Monograph Ser. AGU, Washington D.C., pp. 195–214.

Kissling, E. W., Ellsworth, W. L., Eberhard-Philipps, D., Kradolfer, U., 1994. Initial reference model in local earthquake tomography. J. Geophys. Res. 99, 19,636–19,646.

Kraft, T., Wassermann, J., Igel, H., 2006. High-precision relocation and focal mechanism of the 2002 rain-triggered earthquake swarms at Mt Hochstaufen, SE Germany. Geophys. J. Int. 167, 1513–1528.

Lange, C. D., Rietbrock, A., Haberland, C., Bataille, K., Dahm, T., Tilmann, F., Flüh, E. R., 2007. Seismicity and geometry of the South-Chilean subduction zone (41.5°S and 43.5 °S): implications for controlling parameters. Geophys. Res. Let. 34.

Lomax, A., Virieux, A. J., Volant, P., Berge, C., 2000. Probabilistic earthquake location in 3D and layered models: Introduction of a Metropolis-Gibbs method and comparison with linear locations. In: Thurber, C. H., Rabinowitz, N. (Eds.), Advances in Seismic Event Location. Kluwer, Amsterdam, pp. 101–134.

McKenzie, D., Jackson, J., Priestley, K., 2005. Thermal structure of oceanic and continental lithosphere. Earth

Planet. Sci. Let. 233, 337–349.
Mueller, S., Spence, W., Choy, G. L., 1996. Inelastic models of lithospheric stress—II. Implications for outer-rise seismicity and dynamics. Geophys. J. Int. 125, 54–72.
Nadeau, R. M., Johnson, L. R., 1998. Seismological studies at Parkfield VI: Moment release rates and estimates of source parameters for small repeating earthquakes. Bul. Seism. Soc. Am. 88 (3), 790–814.
Ottemöller, L., Havskov, J., 2003. Moment magnitude determination for local and regional earthquakes based on source spectra. Bul. Seism. Soc. Am. 93 (1), 203–214.
Peacock, S. M., 2001. Are the lower planes of double seismic zones caused by serpentine dehydration in subducting oceanic mantle? Geology 29 (4), 299–302.
Priestley, K., McKenzie, D., 2006. The thermal structure of the lithosphere from shear wave velocities. Earth Planet. Sci. Let. 244, 285–301.
Ranero, C. R., Morgan, J. P., McIntosh, K., Reichert, C., 2003. Bending-related faulting and mantle serpentinization at the Middle America trench. Nature 45, 367 – 373.
Ranero, C. R., Sallares, V., 2004. Geophysical evidence for hydration of the crust and mantle of the Nazca plate during bending at the north Chile trench. Geology 32 (7), 549–552.
Reyners, M., Eberhart-Philipss, D., Stuart, G., 2007. The role of fluids in lower-crustal earthquakes near continental rifts. Nature 446, 1075–1078.
Robin, P.-Y., Robin, C., 2007. Stress trajectories in descending lithospheric slabs and the consequent water cycle. In: Geophys. Res. Abs. Vol. 9. European Geosciences Union 2007, p. 10889.
Robinson, R., McGinty, P., 2000. The enigma of the Arthur's Pass, New Zealand, earthquake 2. The aftershock distribution and its relation to regional and induced stress fields. J. Geophys. Res. 105, 16139–16150.
Rüpke, L. H., Morgan, J. P., Hort, M., Connolly, J. A. D., 2004. Serpentine and the subduction zone water cycle. Earth Planet. Sci. Let. 223, 17–34.
Scherwath, M., Flueh, E., Grevemeyer, I., Tilmann, F., Contreras-Reyes, E., Weinrebe, W., 2006. Investigating subduction zone processes in Chile. EOS American Geophys. Union Trans. 87 (27), 265.
Spičák, A., Horálek, J., 2001. Possible role of fluids in the process of earthquake swarm generation in the West Bohemia/Vogtland seismoactive region. Tectonophys. 336 (1-4), 151–161.
Taylor, M. J., Zheng, G., Rice, J. R., Stuart, W. D., Dmowska, R., 1996. Cyclic stressing and seismicity at strongly coupled subduction zones. J. Geophys. Res. 101 (B4), 8363–8381.
Tichelaar, B. W., Christensen, D. H., Ruff, L. J., 1992. Depth extent of rupture of the 1982 Chilean outer-rise earthquake as inferred from long-period body waves. Bul. Seism. Soc. Am. 82 (3), 1236–1252.
Tilmann, F., Flueh, E., Planert, L., Reston, T., Weinrebe, W., 2004. Microearthquake seismicity of the Mid-Atlantic Ridge at 5°S: A view of tectonic extension. J. Geophys. Res. 109, B06102.
Toomey, D. R., Solomon, S. C., Purdy, G. M., Murray, M. H., 1988. Microearthquakes beneath the median valley of mid-atlantic ridge near 23°N: tomography and tectonics. J. Geophys. Res. 93, 9063–9112.
Turcotte, D. L., Schubert, G., 2002. Geodynamics, 2nd Edition. Cambridge University Press.
Utsu, T., 1992. On seismicity. In: Report of the Joint Research Institute for Statistical Mechanics. Institute for Statictical Mathematics, Tokyo, pp. 139–157.
Vidale, J. E., Boyle, K. L., Shearer, P. M., 2006. Crustal earthquake bursts in California and Japan: Their patterns and relation to volcanoes. Geophys. Res. Let. 33, L20313.
Waldhauser, F., Ellsworth, W. L., 2000. A double-difference earthquake location algorithm. Bul. Seism. Soc. Am. 90, 1353–1368.
Wiemer, S., Wyss, M., 2002. Mapping spatial variability of the frequency-magnitude distribution of earthquakes. In: Dmovska, R. (Ed.), Advances in Geophysics. Vol. 45. Elsevier, pp. 259–302.
Wiens, D. A., Stein, S., 1983. Age dependence of oceanic intraplate seismicity and implications for lithospheric evolution. J. Geophys. Res. 88 (B8), 6455–6468.
Yamashita, T., 1999. Pore creation due to fault slip in a fluid-permeated fault zone and its effect on seismicity: generation mechanism of earthquake swarm. Pure Appl. Geophys. 155, 625–647.

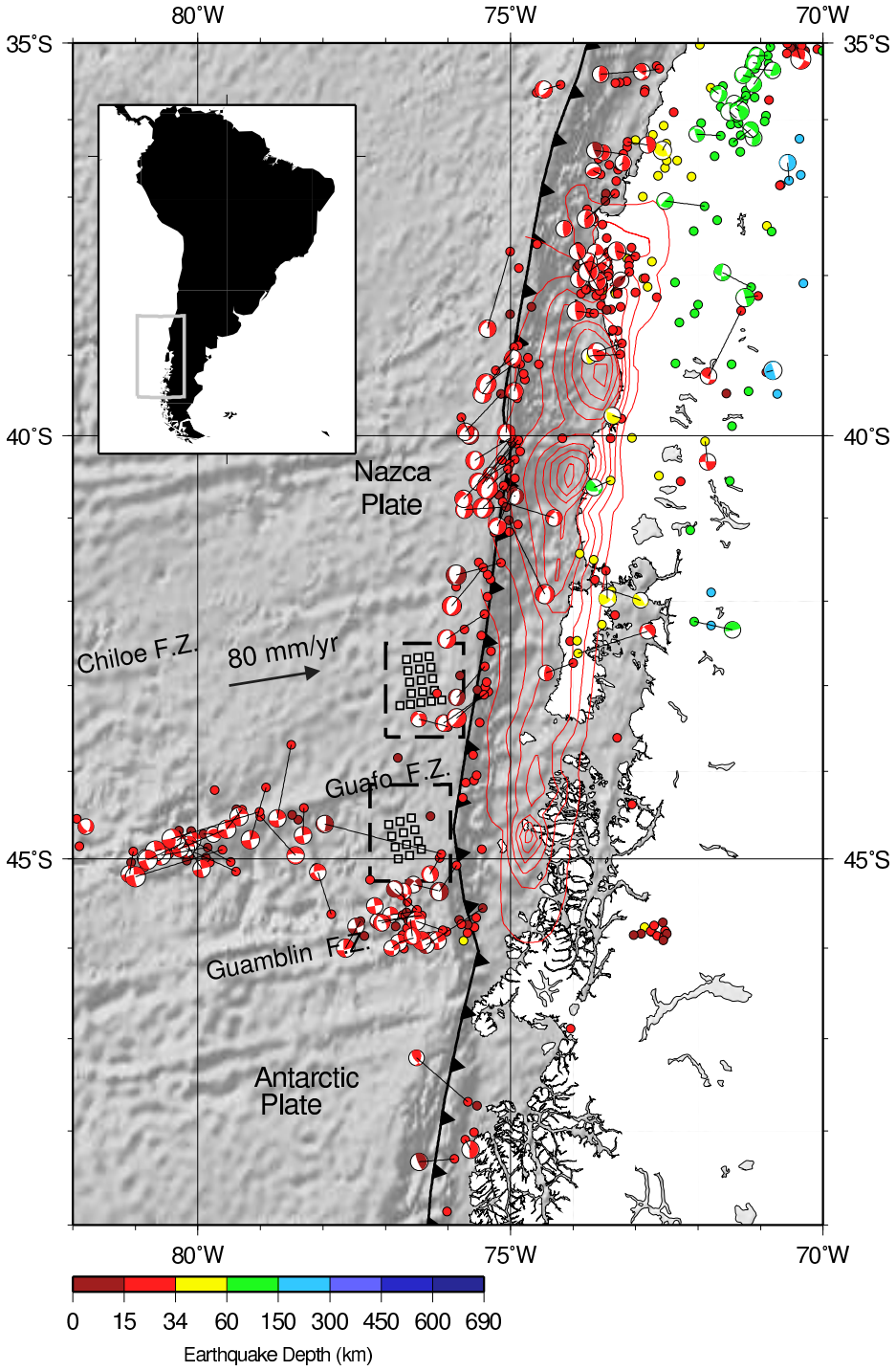

Fig. 1. Seismicity around and north of the Chile triple junction. Focal mechanisms from the Global CMT catalogue are plotted at the centroid location (Dziewonski et al., 1981). Circles show Engdahl solutions (Engdahl et al., 1998), with thin lines connecting CMT and Engdahl locations. Contour lines show presumed coseismic slip of the 1960 Chile earthquake based on geodetic data (Barrientos and Ward, 1990), contour spacing 5 m except for outermost contour, which corresponds to slip of 1 m (contours downdip of the main rupture, which are most likely associated with foreshocks and postseismic creep, not shown). White squares correspond to station locations of the two outer rise arrays. Marked fracture zones indicate segmentation of the incoming Nazca plate.

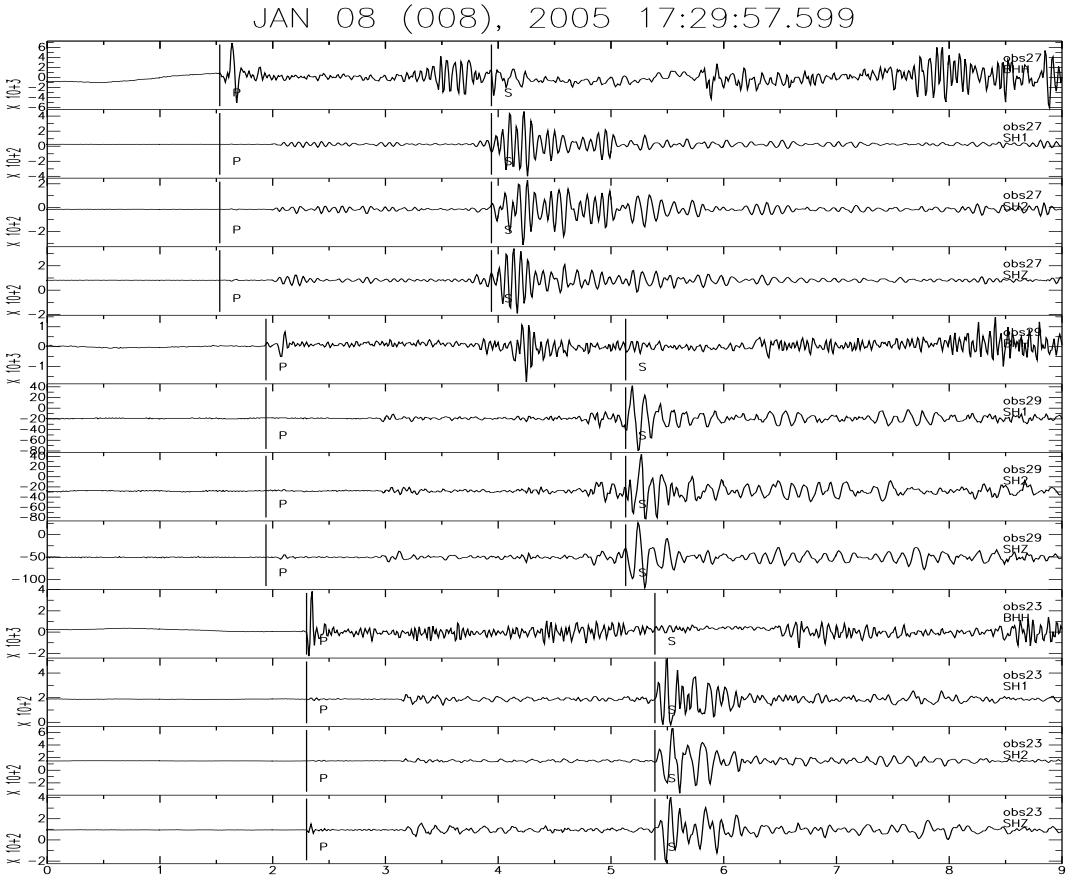

Fig. 2. Waveform example for $M_0 = 1.4 \times 10^{11}$Nm ($M_W = 1.4$) event recorded at stations obs27, obs29 and obs23 of the southern array, all at a water depth of approximately 3250 m. BHH: pressure; SH1, SH2: horizontal components; SHZ: vertical component. A time of 0 s corresponds to the inferred origin time of the event. Picked P and S arrival times are marked by vertical lines. The phase arriving between 6 and 6.5 s is the P wave water multiple; the phase arriving between 7.5 and 8.5 s is the S-converted-to-P water multiple.

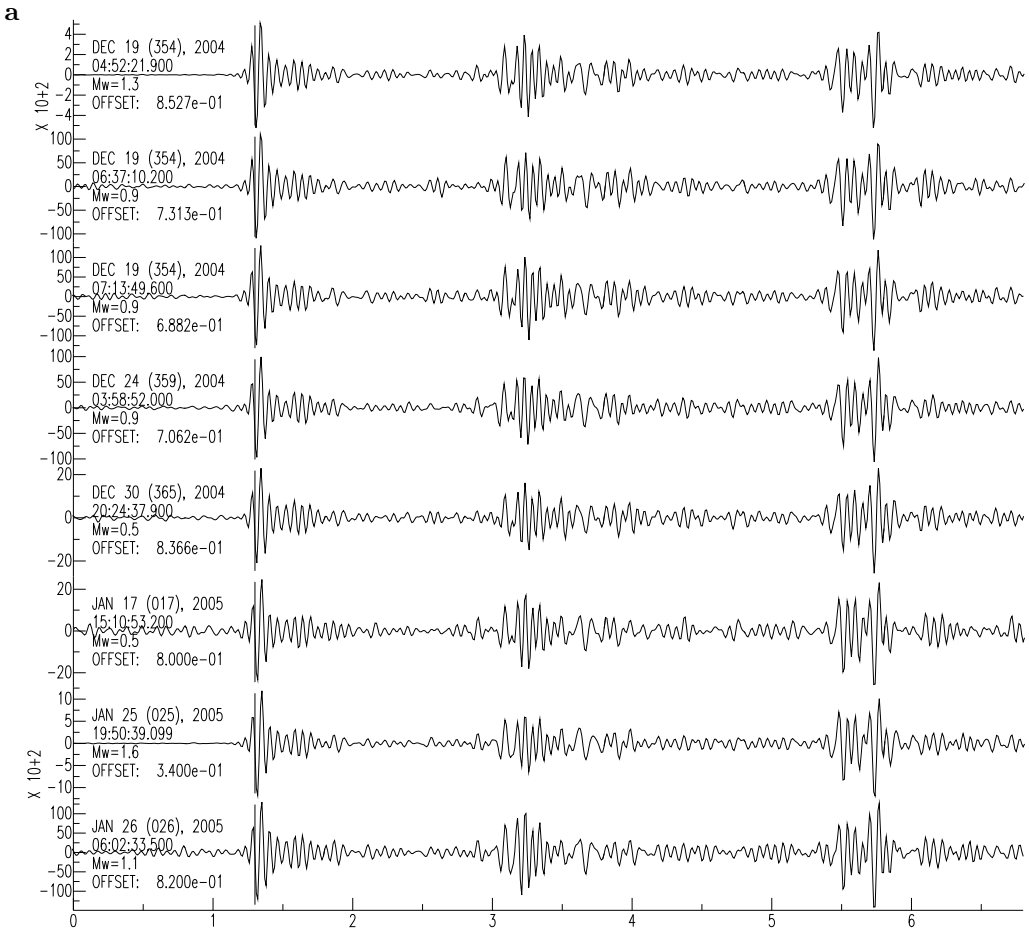

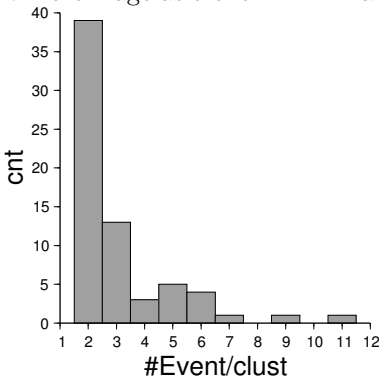

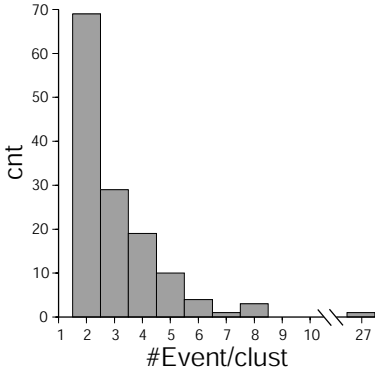

Fig. 3. (a) Waveform example for 8-event cluster in the southern array. Each trace shows the pressure trace from obs24, bandpass filtered 5-20 Hz, with the time axis origin corresponding to the origin time of the earthquake. Event magnitude is estimated from relative amplitudes and the absolute magnitude estimate for the largest event of the cluster. (b), (c) Histograms of number of events per cluster for the northern (b) and southern (c) array. Additionally, the southern array had one cluster consisting of 27 events.

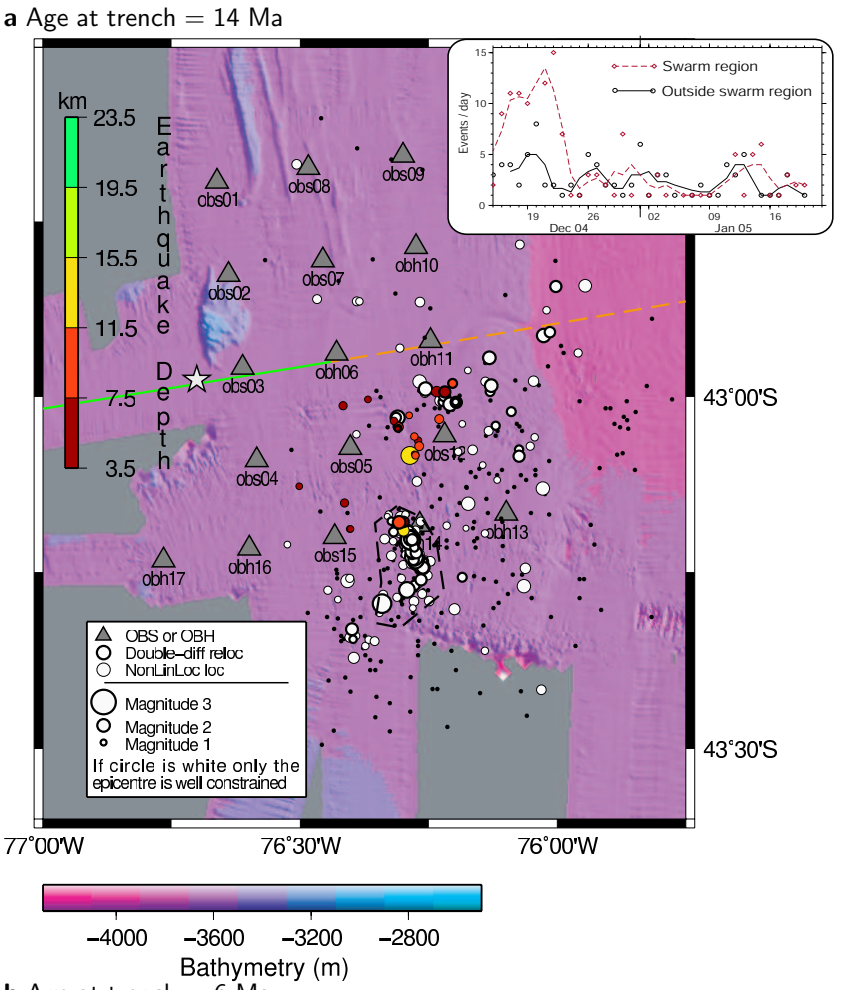
a Age at trench = 14 Ma
km
23.5
19.5
15.5
11.5
7.5
3.5
Earthquake Depth
obs01
obs08
obs09
obs02
obs07
obh10
obh06
obh11
obs03
obs12
obs04
obs05
obh13
obs15
obh16
obh17
OBS or OBH
Double–diff reloc
NonLinLoc loc
Magnitude 3
Magnitude 2
Magnitude 1
If circle is white only the epicentre is well constrained
Swarm region
Outside swarm region
Events / day
Dec 04
Jan 05
77°00'W
76°30'W
76°00'W
43°00'S
43°30'S
–4000
–3600
–3200
–2800
Bathymetry (m)

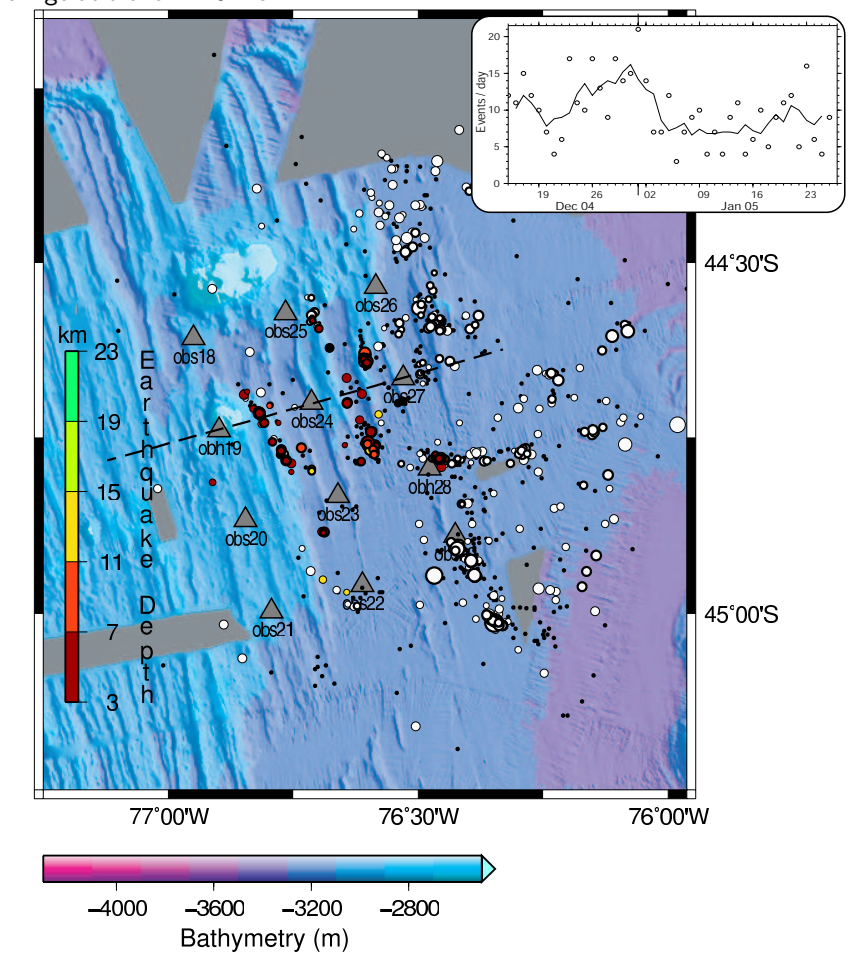
b Age at trench = 6 Ma
km
23
19
15
11
7
3
Earthquake Depth
obs18
obs25
obs26
obs27
obs24
obh19
obh28
obs23
obs20
obs22
obs21
Events / day
Dec 04
Jan 05
77°00'W
76°30'W
76°00'W
44°30'S
45°00'S
–4000
–3600
–3200
–2800
Bathymetry (m)

Fig. 4.

Fig. 4. Epicentral map of events located within the northern array (a) (recording period: 13 Dec 2004 - 22 Jan 2005) and southern array (b) (recording period: 14 Dec 2004 - 27 Jan 2005). Where available, locations resulting from double difference relocation are shown (circles with thick borders), otherwise maximum likelihood locations from the non-linear algorithm are used (circles with thin borders). The earthquake depth color scale is defined relative to sealevel but the color scales for a and b were chosen in such a way that the same depths below the seafloor will approximately correspond to the same color for both arrays. Events with poor depth determination are shown in white. Events recorded by only three or four stations, or where one phase type was missing (P or S) have large epicentral errors and are shown as black dots; no magnitude was determined for these poorly located events. The shaded bathymetry is derived from shipboard soundings during Sonne cruise SO181. In (a), the dashed outline shows the "swarm region" (see text), and the star shows the location where anomalously low heatflow was measured (Contreras-Reyes et al., 2007); a refraction profile was shot along the line through stations obs03, obh06 and obh11: along the green continuous section of the profile, P_n velocity is larger than 8.1 km/s, along the orange dashed section, P_n velocity is 7.8 km/s (Contreras-Reyes et al., 2007). In (b), the dashed line indicates the location of the cross-section in Figure 6. Insets show the daily event rates (actual values and 7-point moving averages); only events in the restricted set with magnitude determinations are taken into account.

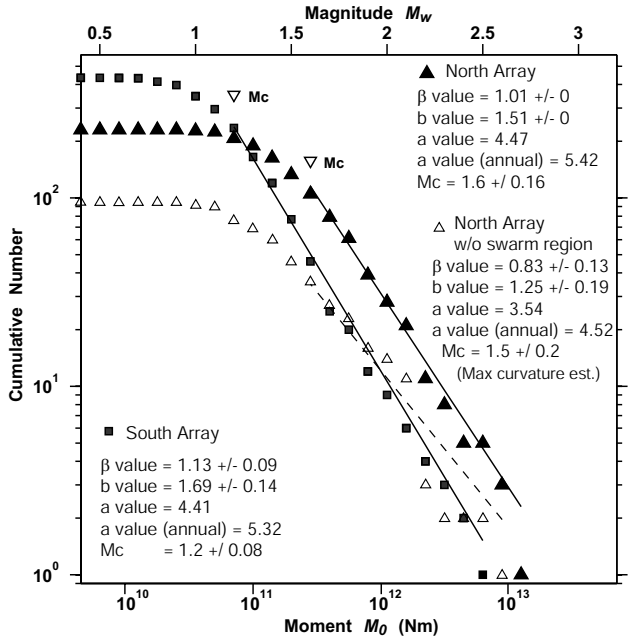

Fig. 5. Frequency-magnitude plots (bottom x axis: $\log_{10} M_0$, top x axis: M_W). The β values were estimated using the maximum likelihood method (Aki, 1965) where the magnitude of completeness was determined using the goodness-of-fit criterion at the 90% level (Wiemer and Wyss, 2002). The southern array is characterized by a larger b value and lower magnitude of completeness M_c but the difference between the β values of the two arrays is not significant according to the Utsu (1992) test. The figure also shows the frequency-magnitude plot for the northern array, when all events within the area of the suspected swarm are excluded. The difference between the β value for this set and the southern array is marginally significant (94% confidence).

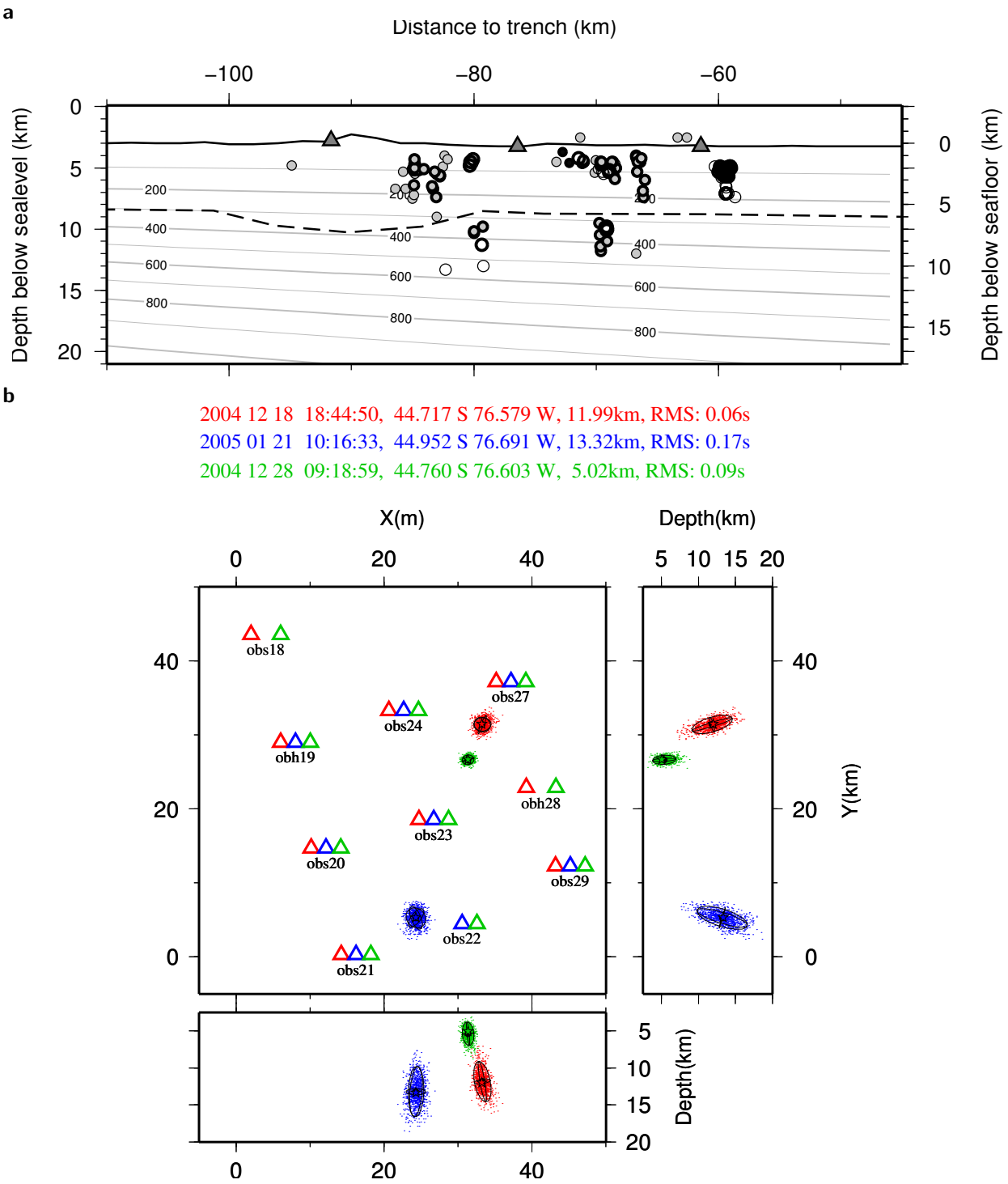

Fig. 6. (a) True-scale cross-section of events with robust depth determinations along profile line through the southern array. (The profile is approximately perpendicular to the spreading direction, see Fig. 4b). Contours show 100°C increments; the temperature field is derived from McKenzie et al.'s (2005) plate cooling model with the asthenospheric potential temperature adjusted to 1280°C, which is required to produce the observed 5 km thick crust. Grey circles indicate earthquakes within 10 km of the profile line, open circles correspond to earthquakes to the south of this swath, and black circles to earthquakes to the north. Circles with thicker borders indicate events which are parts of clusters relocated by the double-difference method. The dashed line indicates the Moho as inferred from refraction data (Scherwath et al., 2006). (b) Probabilistic location uncertainties for three representative events. The probability density function for the hypocentre is represented by scatter plots (see Lomax et al., 2000); the projection of the 95% confidence ellipsoid is shown by black lines, the expectation value for the hypocentre by a black circle, and the maximum likelihood solution by coloured stars (stars and circles overlap to a large degree for all events shown). The coloured triangles indicate the set of stations, at which arrivals have been picked for the three events.

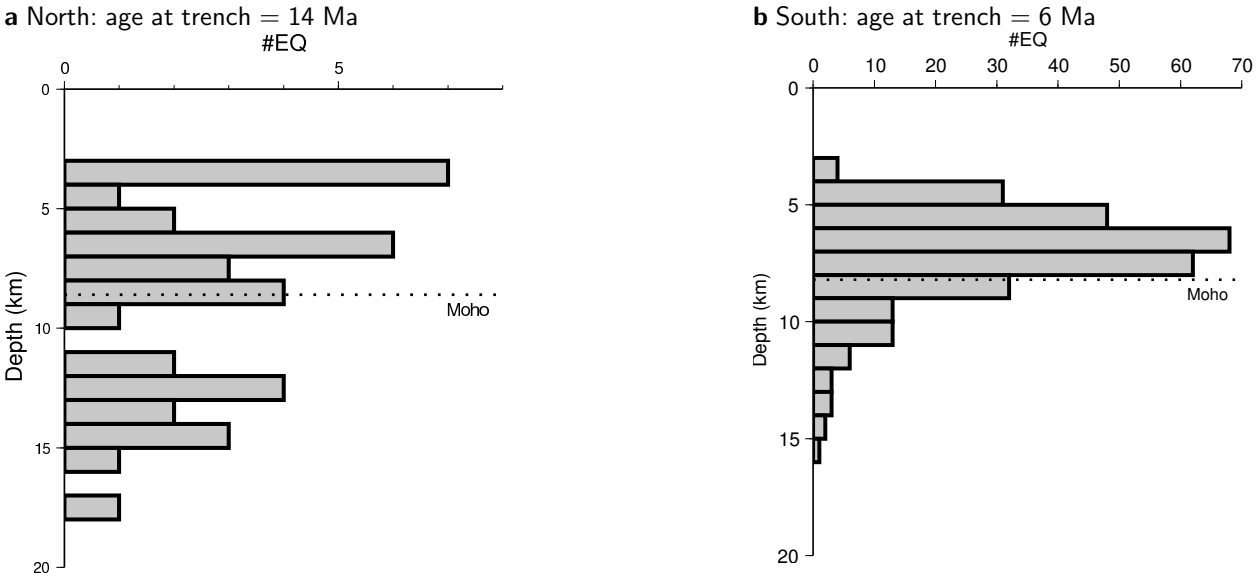

Fig. 7. Depth distribution of events with Gap<200° after joint hypocentre determination in the north (a), and minimum 1-D model inversion in the south (b). The dashed line shows the approximate Moho depth based on refraction profiles. Not all individual earthquakes represented in the histograms are necessarily well constrained, as is apparent from the bundling of events at 3 km in (a) but nearly identical depth distributions were obtained for a large variety of initial models and trial depths in the south (b). As the number of earthquakes in the north is insufficient for a minimum 1D model inversion, the resulting depth distribution is somewhat dependent on the input model. However, the actual input model is well constrained from active source data, and the increased incidence of deeper earthquakes in the north is found for all reasonable models.

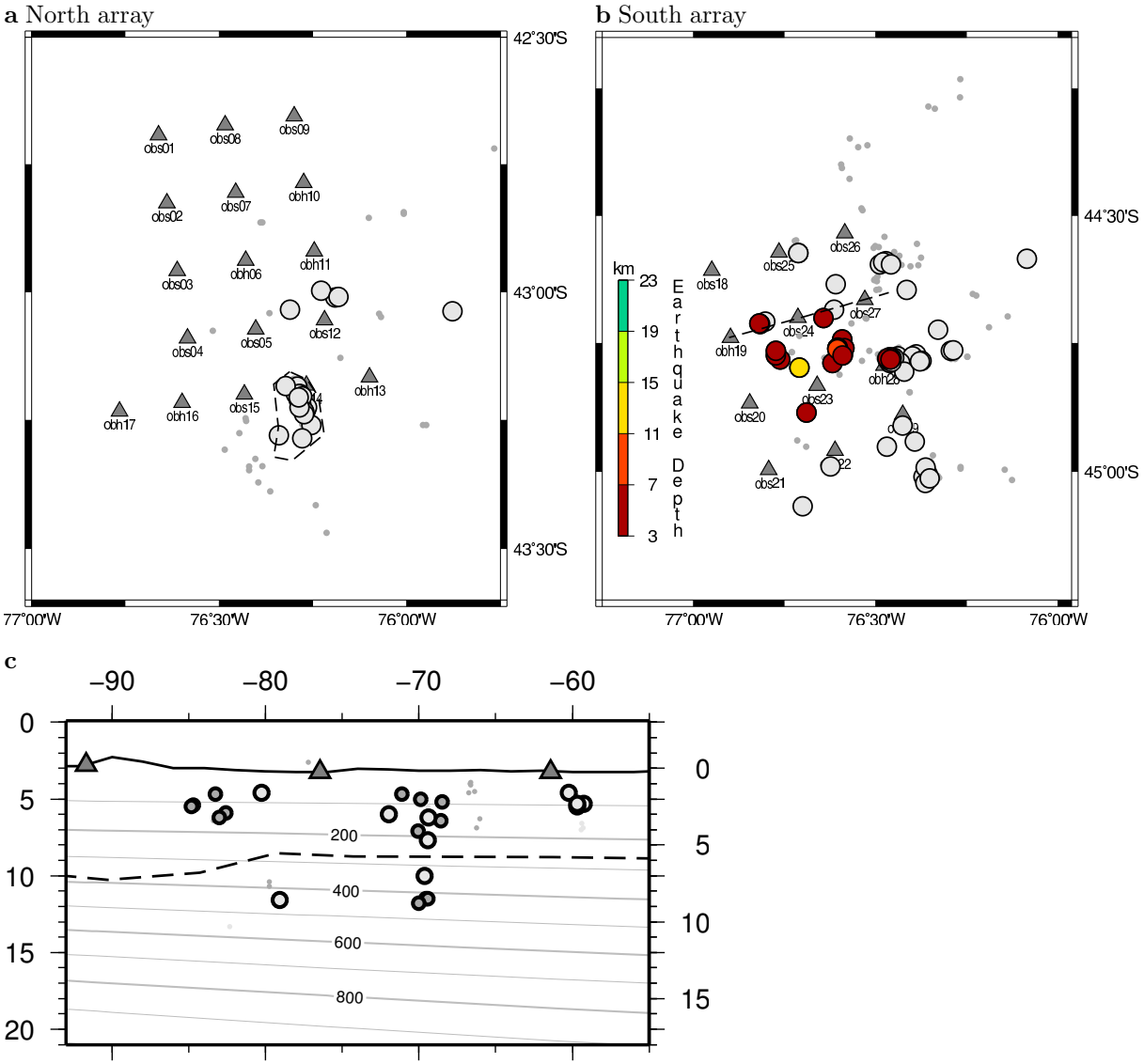

Fig. 8. (a),(b) Epicentral distribution of doublet members (grey dots) and cluster centres for clusters with three or more events (circles). The cluster centres are determined from the medians of the manual picks in stacked waveforms; for a few clusters, these procedure failed because there were not a sufficient number of common picks between the cluster member events. For these clusters and all doublets, instead the member events are shown as grey dots. Where cluster centre depths are well determined, the circles are filled appropriately. (c) Cross-section of clusters and member events for the southern array. Only those events and clusters with well-constrained depths are shown. The profile location is shown as a dashed line in (b).

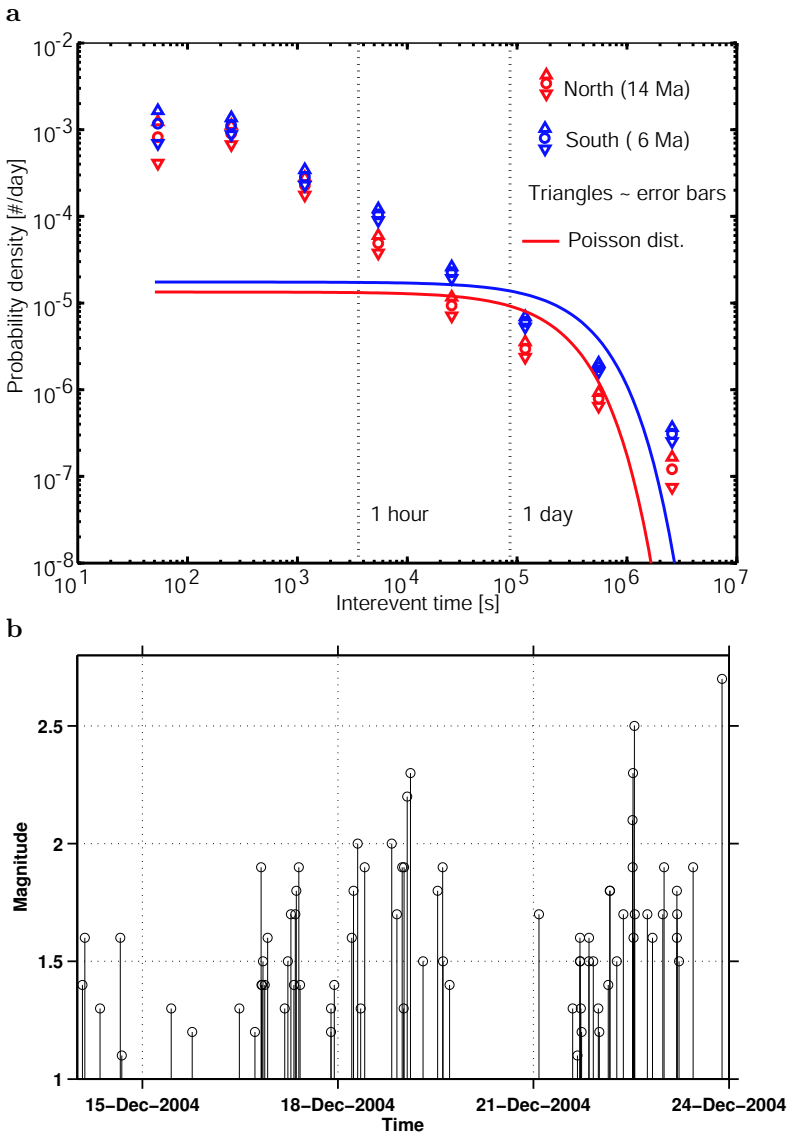

Fig. 9. (a) Probability density distribution of waiting times for all clustered events. Events are binned by inter-event times within the same cluster with logarithmically scaled bin edges; each doublet contributes one waiting time. One standard deviation error bounds are estimated to be proportional to $\sqrt{n}$ where n is the number of waiting times in the bin; this variance estimate would only be strictly correct if the underlying distribution were Poissonian. The continuous line shows the Poisson distribution for a hypothetical cumulative event rate equal to the combination of all clustered events; i.e. the total number of events per day, equivalent to the total area underneath the curve (as it would appear with linear axes), is the same for the actual distribution and the hypothetical Poisson distribution. (b) Magnitude-time plot for the presumed swarm near the northern array; the swarm region is marked in Figure 4.

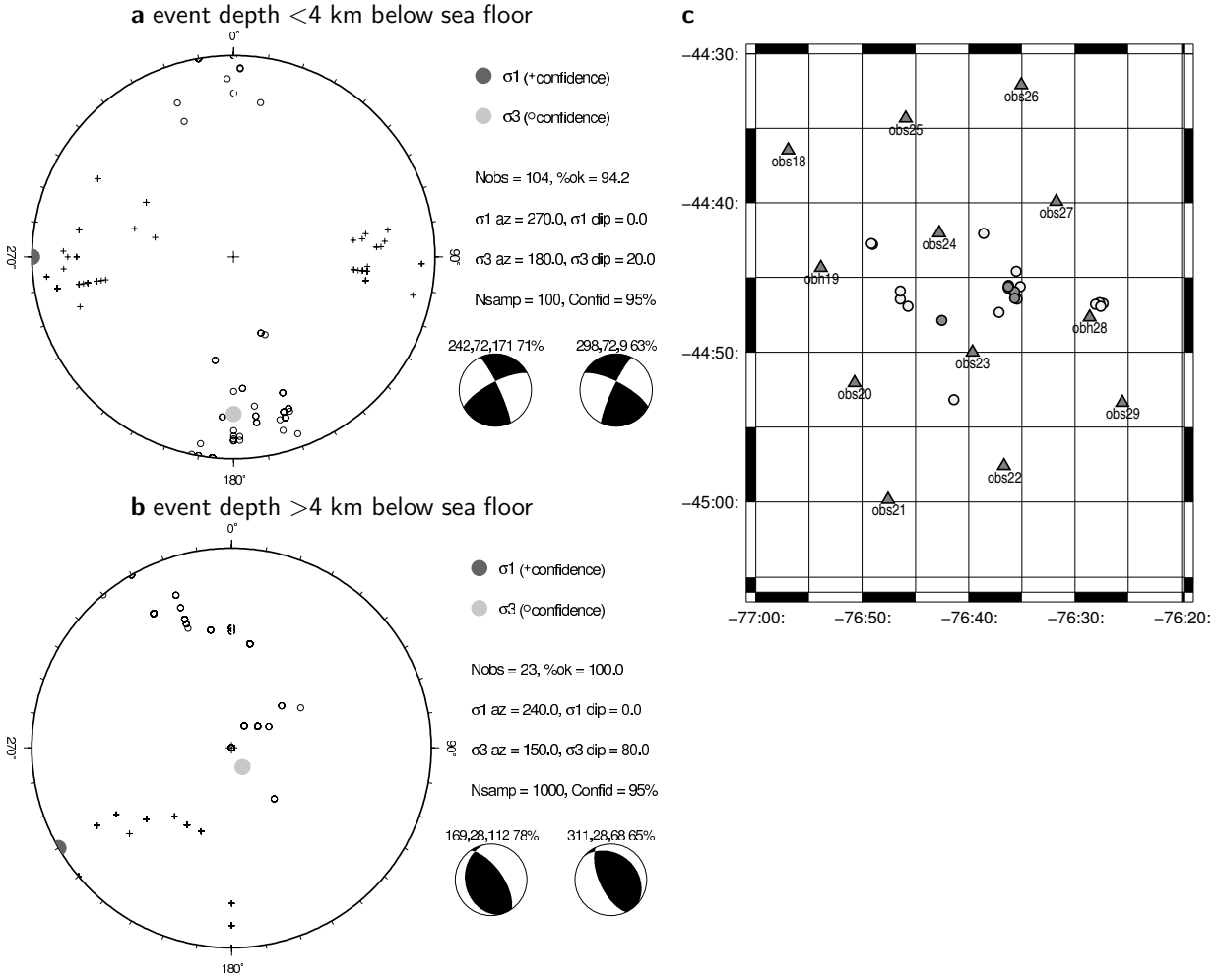

Fig. 10. Upper hemisphere regional pressure and tension axis directions derived from first motions using the Robinson and McGinty (2000) method. The black circle shows the pressure direction (σ_1) and the grey circle the tension direction (σ_3), with noughts and crosses indicating the 95% confidence region. Small beachballs show the expected focal mechanisms for the two optimal fault planes (assuming a coefficient of friction $\mu = 0.75$ in the Coulomb fracture criterion), with the numbers above signifying its strike, dip and rake, and the proportion of first motions consistent with it. (c) Map of cluster locations used in the shallow (light grey circles) and deep (dark grey circles) stress inversions.

Supplementary material

Appendix A. Timing corrections and relocations

(i) The internal clocks of the dataloggers were synchronized with GPS time just before deployment and just after recovery. The internal time was then corrected assuming linear drift. Although there is no way to directly check the linearity assumption it is believed to be a good one, as for any particular clock the deviation from the nominal rate is primarily dependent on temperature which is nearly constant at the seafloor, and the time spent on deck and sinking or rising, during which large temperature variations can be experienced, is short compared to the time on the seafloor.

Typical total drift was less than 100 ms although a few stations had larger drift values. One station (obs20) had experienced a time jump of over 7 s; the drift of this station was determined from the slope of a plot of double-difference times of highly correlated events against the inter-event time (Figure S1). After correction, this slope is nearly zero; and inspection shows that the jump occurred before any events had been recorded.

(ii) Where a refraction profile passed directly over the station, the stations were relocated in the profile-parallel direction by fitting the water wave arrival times from airgun shots near the station. This was the case for all stations except obs05, obs07, obs08 (northern array) and obs18, obh19, obs20, obs21, obs26, obs27, obh28, obs29 (southern array).

Appendix B. Earthquake magnitude determination

Because of the low gain of the seismometer components, and the fact that both vertical and horizontal seismometer components are dominated by shear waves (or p-converted S-waves), whose amplitudes are stronly dependent on site resonance effects (as can be seen from the 'ringy' waveform), we based all our magnitude estimates on hydrophone data. We removed the nominal hydrophone response (Table S2), and then multiplied by ρv_P where v_P and ρ are the sound velocity (1.5 km/s) and density (1000 kg/m^3) of water, respectively. The resulting trace would be identical to the displacement for a vertically incident wave and zero impedance contrast between water and seafloor. These assumptions are not fulfilled exactly but are not violated too badly because velocities and densities of the uppermost sediments are only slightly larger than in the water, and the low velocities cause most earthquake arrivals to have steep raypaths below the receiver.

'Pseudo-displacement' spectra were then calculated from the converted traces for 2 s windows centred on the P wave arrival time. Following standard seismological procedure we assume the Brune (1970) source model, which predicts the frequency-dependent theoretical displacement spectrum $d(f)$ for a circular source at station i:

$$d_i(f) = \frac{KG(r_i,h)A_i(f)}{4\pi\rho v^3}\frac{M_0}{(1+f^2/f_0^2)}S_i \qquad \text{(B.1)}$$

where ρ and v are the density and velocity of the medium ($\rho = 2.8\text{g/cm}^3$, $v_p = 6.2\text{km/s}$), $G(r_i,h)$ the geometrical spreading factor for a source at epicentral distance r_i and depth h ($G(r_i,h) = \sqrt{r_i^2+h^2}$, i.e. body wave spreading is assumed), $A(f) = \exp[-\pi f Q(\kappa + T_i/Q)]$ is the attenuation factor with κ parameterising the near-receiver attenuation ($\kappa = 0.015$), T_i being the travel time and Q the quality factor ($Q_P = 400$ with a slight assumed frequency dependence). K is a factor correcting for the radiation pattern and free surface effect; usually this is set to $2 * 0.6$ where 0.6 is the radiation pattern effect averaged over the focal sphere, and 2 corrects for the free surface effect. Instead, we set K to 0.6 as the seismic stations are effectively imbedded in the media. S_i is a station term to account for site specific amplification or differences in media properties; initially all station terms are set to 0.

Moment magnitude estimates for each station are then automatically generated by a genetic algorithm which searches for the combination of seismic moment M_0 and corner frequency f_0 that best fits the observed spectrum corrected for attenuation and geometric spreading, using the method and code of Ottemöller and Havskov (2003). We only make use of frequencies above 4 Hz; as lower frequencies were dominated by noise for all but the largest events, and the lower limit is still likely to be above the corner frequency of all events. Corner frequency measurements are discarded as corner frequencies of most events are close to or larger than the Nyquist frequency, and moment magnitudes derived from the moments according to Kanamori (1977). Finally, the individual station moment magnitudes estimates are combined in order to estimate the station terms and final earthquake moment magnitudes under the constraint that the geometric average of the station terms S_i be 1 (equivalently ($\sum_i \log_{10} S_i = 0$). The standard deviation of $\log_{10} S_i$ is 0.43 for the southern array and 0.27 for the northern array (except obh10, see table S2), where this variation is likely dominated by site effects, e.g. variations in seafloor impedance contrast and sedimentary layer thickness. Formal uncertainties of individual $\log_{10} s_i$ values are around 0.05 and

formal uncertainties of average event moment magnitudes are around 0.1 magnitude units. A total of four events located by the northern array were also located by a contemporary land deployment (Lange et al., 2007). The land magnitudes, which are based on the Richter magnitude formula and are generally close to magnitudes in the NEIC catalogue, are on average 0.35 magnitude units larger than the ocean bottom magnitudes but because this comparison is based on two different magnitude scales and involves events located far from the array, where the geometrical spreading and attenuation functions might no longer be appropriate, we did not correct the ocean bottom magnitudes for this potential bias. No events in the catalogue of the southern array have been recorded on land, and only two events have magnitude determinations from stations of both arrays; these two events appear to be 0.4-0.5 magnitudes larger in the northern array. Invariably, these events are far away from one of the arrays such that it cannot be determined whether the difference can be attributed to differences in the average station terms of both arrays, or to inappropriate spreading/attenuation assumptions for more distant events, and any conclusion based on a comparison of just two events must remain highly uncertain in any case.

Table S1
List of stations

Station	Lat	Lon	Depth	Instrument[1]		Statics (s)		Pobs	Sobs	$\log_{10} S_i$
	°S	°W	(m)	Hydr	Seism	P	S	#	#	[1]
North array: age at trench = 14 Ma										
obs01	42.6923	76.6613	3543	OAS	Webb	0.56	0.74	76	7	-0.02
obs02	42.8258	76.6390	3526	OAS	Owen 4.5Hz	0.31	0.33	112	9	0.18
obs03	42.9590	76.6118	3537	OAS	Owen 4.5Hz	0.21	0.76	271	283	0.26
obs04	43.0908	76.5847	3524	DPG	Webb	0.02	0.32	263	267	—
obs05	43.0732	76.4025	3566	OAS	Owen 4.5Hz	0.03	0.36	551	558	0.05
obh06	42.9388	76.4288	3559	OAS	—	0.21	—	139	—	—
obs07	42.8052	76.4557	3555	OAS	Owen 4.5Hz	0.48	0.68	200	264	-0.01
obs08	42.6730	76.4837	3553	OAS	Owen 4.5Hz	0.30	0.72	102	48	—
obs09	42.6553	76.3002	3590	DPG	Webb	0.42	0.93	80	47	—
obh10	42.7863	76.2743	3627	OAS	—	0.47	—	137	—	2.03
obh11	42.9203	76.2467	3616	OAS	—	0.28	—	166	—	0.03
obs12	43.0553	76.2193	3590	OAS	Webb	-0.04	0.70	491	311	—
obh13	43.1668	76.0993	3613	OAS	—	-0.63	—	2	—	—
obh14	43.1828	76.2672	3559	OAS	—	-0.28	—	568	—	-0.27
obs15	43.2000	76.4330	3530	OAS	Webb	-0.18	0.22	327	26	—
obh16	43.2165	76.5987	3511	OAS	—	0.02	—	268	—	—
obh17 [2]	43.2333	76.7658	3504	HTI	—	0.00	—	190	—	-0.21
South array: age at trench = 6 Ma										
obs18	44.6080	76.9492	3074	HTI	Owen 4.5Hz	-0.44	0.46	322	242	—
obh19	44.7392	76.8982	2787	HTI	—	-0.57	—	310	—	—
obs20	44.8675	76.8455	3025	OAS	Owen 4.5Hz	-0.56	0.24	428	682	0.44
obs21	44.9972	76.7932	3106	OAS	Owen 4.5Hz	-0.53	0.10	42	288	—
obs22	44.9597	76.6113	3262	OAS	Owen 4.5Hz	-0.33	0.33	363	364	-0.12
obs23	44.8332	76.6608	3237	OAS	Owen 4.5Hz	-0.33	0.41	808	987	-0.04
obs24	44.7005	76.7130	3221	OAS	Owen 4.5Hz	-0.46	0.16	604	762	-0.44
obs25	44.5722	76.7655	3029	HTI	Owen 4.5Hz	-0.50	0.40	17	36	—
obs26	44.5348	76.5845	3017	HTI	Owen 4.5Hz	—	—	—	—	—
obs27	44.6653	76.5298	3240	HTI	Owen 4.5Hz	-0.52	-0.25	536	734	—
obh28	44.7942	76.4772	3255	OAS	—	-0.28	—	565	—	0.37
obs29 [2]	44.8895	76.4260	3263	OAS	Owen	0.00	1.04	470	535	-0.21

[1] The mean of the log amplitude station terms (excluding obh10) is 0 by definition, see text.
[2] The P delay of stations obh17 and obs29 is 0 s by definition. All other station delays are defined relative to the P delay at these two stations.

Table S2
Hydrophone reponse in angular frequency convention for obs 20,22, 23, 29 and 29, and obh 28 (southern array), and obs01, 02, 03, 06 and 07, and obh 10, 11, 14, 16 (northern array)[1].

	Real Im
Poles	0.0 0.0
Zeros	-20.0 0.0
Gain (cnt/Pa)	1050

[1] Subsequent analysis of magnitudes and amplitudes showed that at obh10 amplitudes were larger than expected by a factor of approximately 1000. The amplitude estimates for this station were accordingly corrected by this factor to be more compatible with the remainding stations.

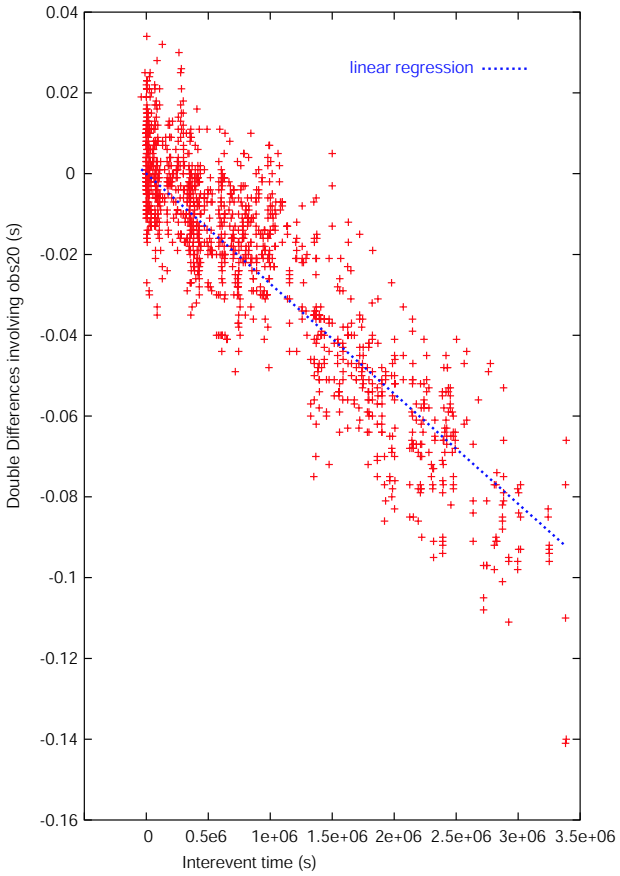

Fig. S1. Double-difference times for similar earthquakes of uncorrected obs20 picks with corrected picks from all other stations plotted versus inter-event time. The double difference times are determined by waveform cross-correlation with a window length of 9.5 s. Because the same slope is obtained for double differences of obs20 with all other stations it is unlikely that the slope represents a spatial trend (e.g. migration of hypocentres); instead, it is due to clock drift at obs20. This conclusion is further supported by the fact that similar plots with other reference stations all appear flat. In contrast, the scatter is probably at least partly due to small changes in event location.

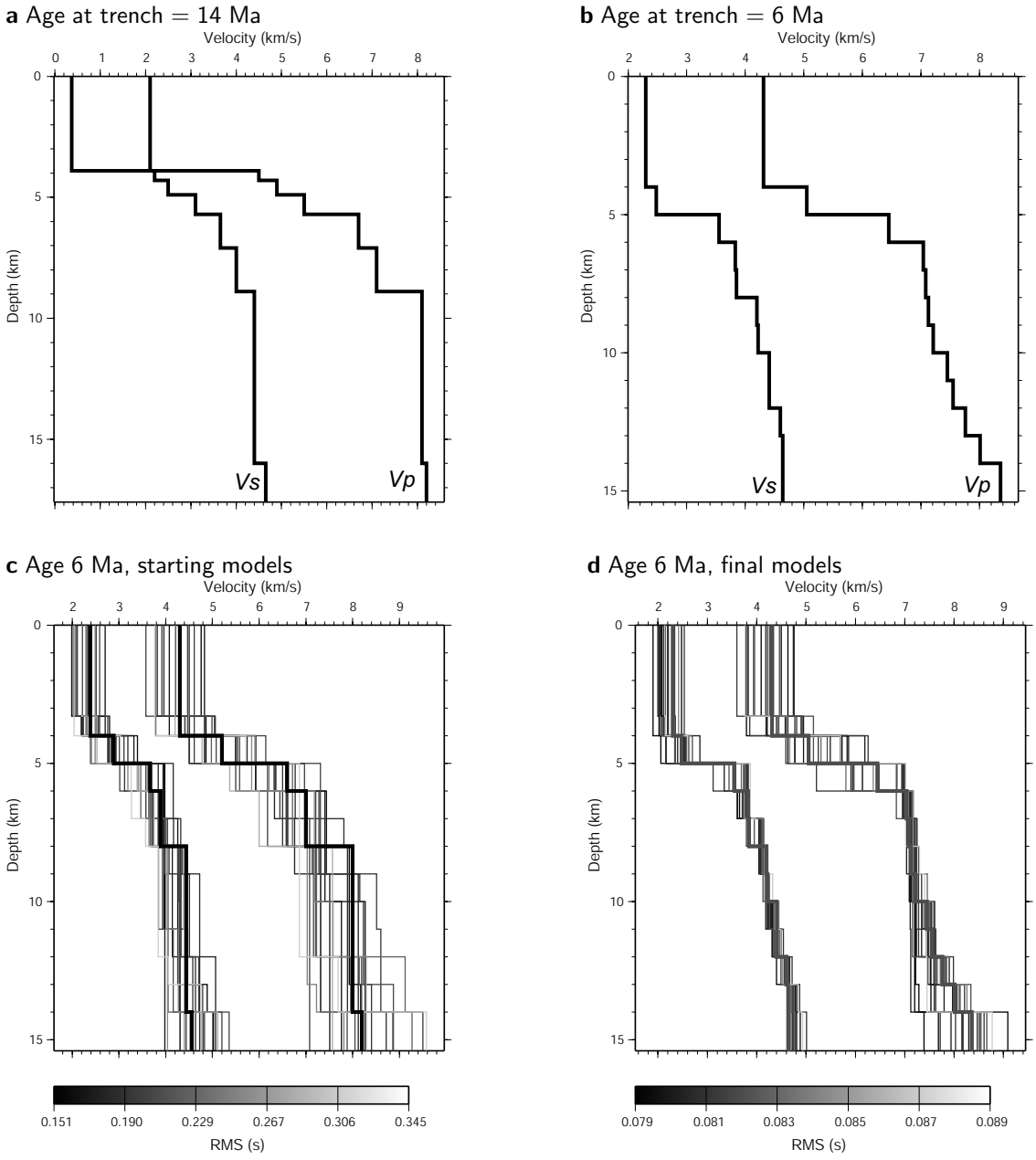

Fig. S2. 1D velocity models used for the final inversion. The model for the northern array (a) is an average of the two-dimensional trench-parallel and -perpendicular models from refraction profiling, and the model for the southern array (b) has been derived by a linearised inversion of the travel time picks from well-located events within the array. A set of 20 inversions with different starting models were run to test the sensitivity of the final model on the starting model: (c) shows the 20 starting models. The shade of the lines indicates the initial rms misfit of the travel time data for the model. The thick line shows the starting model for the preferred model. (d) the final inversion results for the 20 runs are shown. The thick line shows the preferred model (same as (b)). The shade of the lines indicates the final rms misfit.

Supplementary material

A Timing corrections and relocations

(1) The internal clocks of the dataloggers were synchronized with GPS time just before deployment and just after recovery. The internal time was then corrected assuming linear drift. Although there is no way to directly check the linearity assumption it is believed to be a good one, as for any particular clock the deviation from the nominal rate is primarily dependent on temperature which is nearly constant at the seafloor, and the time spent on deck and sinking or rising, during which large temperature variations can be experienced, is short compared to the time on the seafloor.

    Typical total drift was less than 100 ms although a few stations had larger drift values. One station (obs20) had experienced a time jump of over 7 s; the drift of this station was determined from the slope of a plot of double-difference times of highly correlated events against the inter-event time (Figure S1). After correction, this slope is nearly zero; and inspection shows that the jump occurred before any events had been recorded.

(2) Where a refraction profile passed directly over the station, the stations were relocated in the profile-parallel direction by fitting the water wave arrival times from airgun shots near the station. This was the case for all stations except obs05, obs07, obs08 (northern array) and obs18, obh19, obs20, obs21, obs26, obs27, obh28, obs29 (southern array).

B Earthquake magnitude determination

Because of the low gain of the seismometer components, and the fact that both vertical and horizontal seismometer components are dominated by shear waves (or p-converted S-waves), whose amplitudes are stronly dependent on site resonance effects (as can be seen from the 'ringy' waveform), we based all our magnitude estimates on hydrophone data. We removed the nominal hydrophone response (Table S2), and then multiplied by ρv_P where v_P and ρ are the sound velocity (1.5 km/s) and density (1000 kg/m^3) of water, respectively. The resulting trace would be identical to the displacement for a vertically incident wave and zero impedance contrast between water and seafloor. These assumptions are not fulfilled exactly but are not violated too badly because velocities and densities of the uppermost sediments are only slightly larger than in the water, and the low velocities cause most earthquake arrivals to have steep raypaths below the receiver.

'Pseudo-displacement' spectra were then calculated from the converted traces for 2 s windows centred on the P wave arrival time. Following standard seismological procedure we assume the Brune (1970) source model, which predicts the frequency-dependent theoretical displacement spectrum $d(f)$ for a circular source at station i:

$$d_i(f) = \frac{KG(r_i,h)A_i(f)}{4\pi\rho v^3}\frac{M_0}{(1+f^2/f_0^2)}S_i \tag{B.1}$$

where ρ and v are the density and velocity of the medium ($\rho = 2.8\text{g/cm}^3$, $v_p = 6.2\text{km/s}$), $G(r_i,h)$ the geometrical spreading factor for a source at epicentral distance r_i and depth h ($G(r_i,h) = \sqrt{r_i^2+h^2}$, i.e. body wave spreading is assumed), $A(f) = \exp[-\pi f Q(\kappa + T_i/Q)]$ is the attenuation factor with κ parameterising the near-receiver attenuation ($\kappa = 0.015$), T_i being the travel time and Q the quality factor ($Q_P = 400$ with a slight assumed frequency dependence). K is a factor correcting for the radiation pattern and free surface effect; usually this is set to $2 * 0.6$ where 0.6 is the radiation pattern effect averaged over the focal sphere, and 2 corrects for the free surface effect. Instead, we set K to 0.6 as the seismic stations are effectively imbedded in the media. S_i is a station term to account for site specific amplification or differences in media properties; initially all station terms are set to 0.

Moment magnitude estimates for each station are then automatically generated by a genetic algorithm which searches for the combination of seismic moment M_0 and corner frequency f_0 that best fits the observed spectrum corrected for attenuation and geometric spreading, using the method and code of Ottemöller and Havskov (2003). We only make use of frequencies above 4 Hz; as lower frequencies were dominated by noise for all but the largest events, and the lower limit is still likely to be above the corner frequency of all events. Corner frequency measurements are discarded as corner frequencies of most events are close to or larger than the Nyquist frequency, and moment magnitudes derived from the moments according to Kanamori (1977). Finally, the individual station moment magnitudes estimates are combined in order to estimate the station terms and final earthquake moment magnitudes under the constraint that the geometric average of the station terms S_i be 1 (equivalently ($\sum_i \log_{10} S_i = 0$). The standard deviation of $\log_{10} S_i$ is 0.43 for the southern array and 0.27 for the northern array (except obh10, see table S2), where this variation is likely dominated by site effects, e.g. variations in seafloor impedance contrast and sedimentary layer thickness. Formal uncertainties of individual $\log_{10} s_i$ values are around 0.05 and formal uncertainties of average event moment magnitudes are around 0.1 magnitude units. A total of four events located by the northern array were also located by a contemporary land deployment (Lange et al., 2007). The land magnitudes, which are based on the Richter magnitude formula and are generally close to magnitudes in the NEIC catalogue, are on average 0.35 magnitude units larger

than the ocean bottom magnitudes but because this comparison is based on two different magnitude scales and involves events located far from the array, where the geometrical spreading and attenuation functions might no longer be appropriate, we did not correct the ocean bottom magnitudes for this potential bias. No events in the catalogue of the southern array have been recorded on land, and only two events have magnitude determinations from stations of both arrays; these two events appear to be 0.4-0.5 magnitudes larger in the northern array. Invariably, these events are far away from one of the arrays such that it cannot be determined whether the difference can be attributed to differences in the average station terms of both arrays, or to inappropriate spreading/attenuation assumptions for more distant events, and any conclusion based on a comparison of just two events must remain highly uncertain in any case.

References

Brune, J., 1970. Tectonic stress and the spectra of seismic shear waves from earthquakes. J. Geophys. Res. 75, 4997–5009.

Kanamori, H., 1977. The energy release in great earthquakes. J. Geophys. Res. 82, 1981–1987.

Lange, C. D., Rietbrock, A., Haberland, C., Bataille, K., Dahm, T., Tilmann, F., Flüh, E. R., 2007. Seismicity and geometry of the South-Chilean subduction zone (41.5°S and 43.5 °S): implications for controlling parameters. Geophys. Res. Let. 34.

Ottemöller, L., Havskov, J., 2003. Moment magnitude determination for local and regional earthquakes based on source spectra. Bul. Seism. Soc. Am. 93 (1), 203–214.

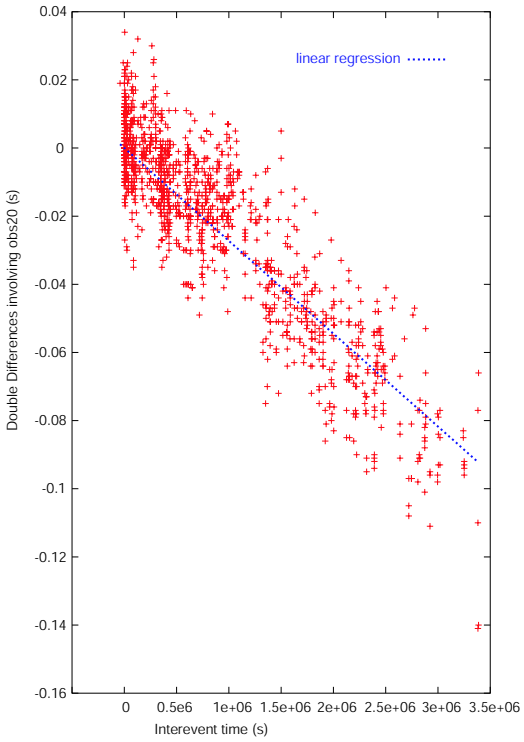

Fig. S1. Double-difference times for similar earthquakes of uncorrected obs20 picks with corrected picks from all other stations plotted versus inter-event time. The double difference times are determined by waveform cross-correlation with a window length of 9.5 s. Because the same slope is obtained for double differences of obs20 with all other stations it is unlikely that the slope represents a spatial trend (e.g. migration of hypocentres); instead, it is due to clock drift at obs20. This conclusion is further supported by the fact that similar plots with other reference stations all appear flat. In contrast, the scatter is probably at least partly due to small changes in event location.

Table S1
List of stations

Station	Lat	Lon	Depth	Instrument[1]		Statics (s)		Pobs	Sobs	$\log_{10} S_i$
	°S	°W	(m)	Hydr	Seism	P	S	#	#	[1]
North array: age at trench = 14 Ma										
obs01	42.6923	76.6613	3543	OAS	Webb	0.56	0.74	76	7	-0.02
obs02	42.8258	76.6390	3526	OAS	Owen 4.5Hz	0.31	0.33	112	9	0.18
obs03	42.9590	76.6118	3537	OAS	Owen 4.5Hz	0.21	0.76	271	283	0.26
obs04	43.0908	76.5847	3524	DPG	Webb	0.02	0.32	263	267	—
obs05	43.0732	76.4025	3566	OAS	Owen 4.5Hz	0.03	0.36	551	558	0.05
obh06	42.9388	76.4288	3559	OAS	—	0.21	—	139	—	—
obs07	42.8052	76.4557	3555	OAS	Owen 4.5Hz	0.48	0.68	200	264	-0.01
obs08	42.6730	76.4837	3553	OAS	Owen 4.5Hz	0.30	0.72	102	48	—
obs09	42.6553	76.3002	3590	DPG	Webb	0.42	0.93	80	47	—
obh10	42.7863	76.2743	3627	OAS	—	0.47	—	137	—	2.03
obh11	42.9203	76.2467	3616	OAS	—	0.28	—	166	—	0.03
obs12	43.0553	76.2193	3590	OAS	Webb	-0.04	0.70	491	311	—
obh13	43.1668	76.0993	3613	OAS	—	-0.63	—	2	—	—
obh14	43.1828	76.2672	3559	OAS	—	-0.28	—	568	—	-0.27
obs15	43.2000	76.4330	3530	OAS	Webb	-0.18	0.22	327	26	—
obh16	43.2165	76.5987	3511	OAS	—	0.02	—	268	—	—
obh17 [2]	43.2333	76.7658	3504	HTI	—	0.00	—	190	—	-0.21
South array: age at trench = 6 Ma										
obs18	44.6080	76.9492	3074	HTI	Owen 4.5Hz	-0.44	0.46	322	242	—
obh19	44.7392	76.8982	2787	HTI	—	-0.57	—	310	—	—
obs20	44.8675	76.8455	3025	OAS	Owen 4.5Hz	-0.56	0.24	428	682	0.44
obs21	44.9972	76.7932	3106	OAS	Owen 4.5Hz	-0.53	0.10	42	288	—
obs22	44.9597	76.6113	3262	OAS	Owen 4.5Hz	-0.33	0.33	363	364	-0.12
obs23	44.8332	76.6608	3237	OAS	Owen 4.5Hz	-0.33	0.41	808	987	-0.04
obs24	44.7005	76.7130	3221	OAS	Owen 4.5Hz	-0.46	0.16	604	762	-0.44
obs25	44.5722	76.7655	3029	HTI	Owen 4.5Hz	-0.50	0.40	17	36	—
obs26	44.5348	76.5845	3017	HTI	Owen 4.5Hz	—	—	—	—	—
obs27	44.6653	76.5298	3240	HTI	Owen 4.5Hz	-0.52	-0.25	536	734	—
obh28	44.7942	76.4772	3255	OAS	—	-0.28	—	565	—	0.37
obs29 [2]	44.8895	76.4260	3263	OAS	Owen	0.00	1.04	470	535	-0.21

[1] The mean of the log amplitude station terms (excluding obh10) is 0 by definition, see text.

[2] The P delay of stations obh17 and obs29 is 0 s by definition. All other station delays are defined relative to the P delay at these two stations.

Table S2
Hydrophone reponse in angular frequency convention for obs 20,22, 23, 29 and 29, and obh 28 (southern array), and obs01, 02, 03, 06 and 07, and obh 10, 11, 14, 16 (northern array)[1].

	Real	Im
Poles	0.0	0.0
Zeros	-20.0	0.0
Gain (cnt/Pa)	1050	

[1] Subsequent analysis of magnitudes and amplitudes showed that at obh10 amplitudes were larger than expected by a factor of approximately 1000. The amplitude estimates for this station were accordingly corrected by this factor to be more compatible with the remainding stations.

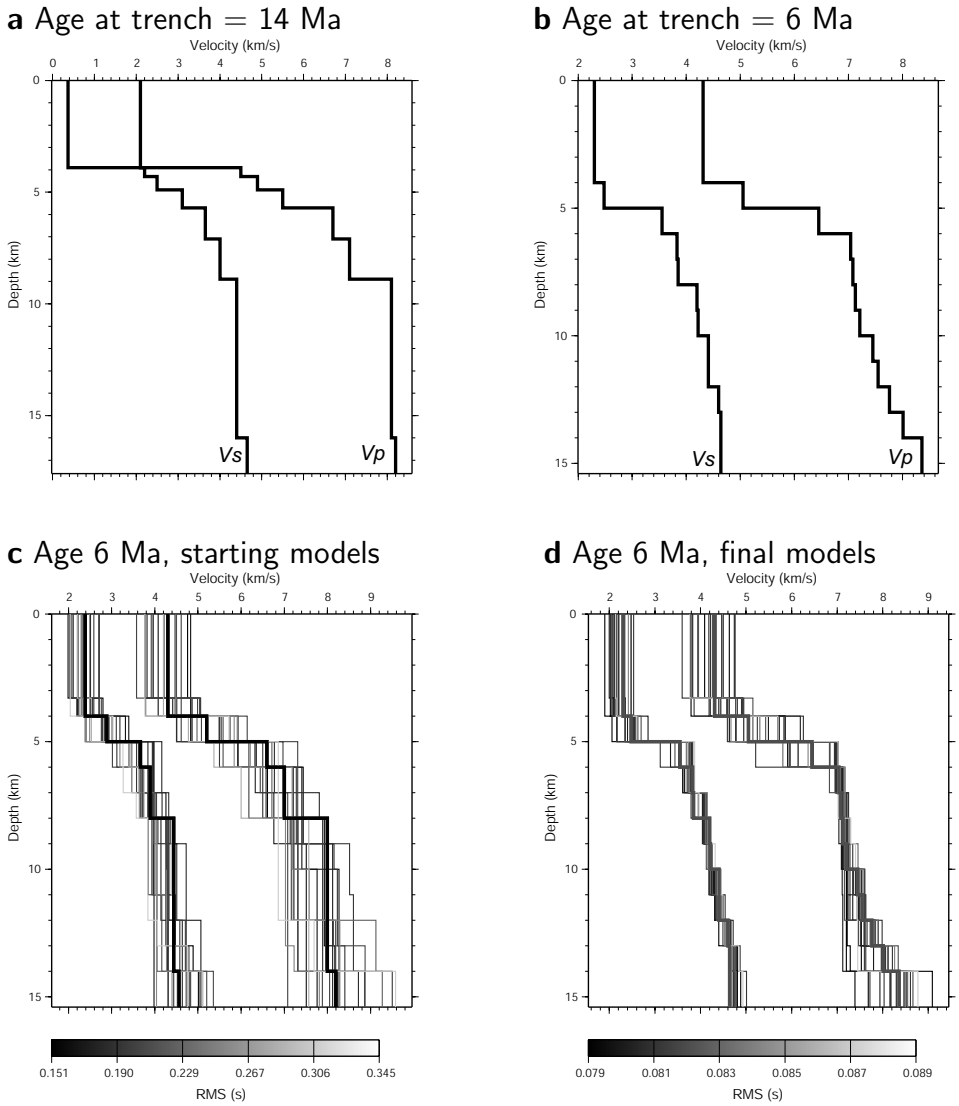

Fig. S2. 1D velocity models used for the final inversion. The model for the northern array (a) is an average of the two-dimensional trench-parallel and -perpendicular models from refraction profiling, and the model for the southern array (b) has been derived by a linearised inversion of the travel time picks from well-located events within the array. A set of 20 inversions with different starting models were run to test the sensitivity of the final model on the starting model: (c) shows the 20 starting models. The shade of the lines indicates the initial rms misfit of the travel time data for the model. The thick line shows the starting model for the preferred model. (d) the final inversion results for the 20 runs are shown. The thick line shows the preferred model (same as (b)). The shade of the lines indicates the final rms misfit.